TU WIEN

DIPLOMARBEIT

Phase Behaviour of a System of Inverse Patchy Colloids: A Simulation Study

Ausgeführt am Institut für

Theoretische Physik

der Technischen Universität Wien

unter der Anleitung von

Ao. Univ. Prof. Dipl.-Ing. Dr. Gerhard Kahl

in Zusammenarbeit mit

Dr. Eva G. Noya

durch

Ismene Kolovos

Wilhelm Kress Gasse 2, 2353 Guntramsdorf

30. April 2013

Abstract

In this thesis, we consider mesoscopic colloidal particles with a negatively charged equatorial region and two positively charged polar caps. We refer to them as "inverse patchy colloids", by which we imply that charge-like regions repel each other, while oppositely charged regions attract each other. We model the system via a recently introduced coarse-grained description and we investigate the effect of the interplay between the directional attractive and repulsive interactions on the equilibrium phase diagram; this includes the disordered fluid phase, two spatially and orientationally ordered lattices as well as a plastic crystal, where the orientation of the particles is almost randomly distributed. Via a combination of evolutionary algorithms (that predict ordered candidate structures at vanishing temperature) and free energy calculation techniques (involving Monte Carlo simulations), we are able to identify the regions of thermodynamic stability of the fluid phase and the three solid structures.

Contents

1. Introduction

In recent years, the investigation of the physical properties of colloidal patchy particles has been of high interest in soft matter physics, with both theoretical and experimental groups putting effort into the topic [1, 2].

Colloids[1] are mesoscopic particles (at the size of some nm to μm) that are suspended in a solvent of microscopic particles. The internal degrees of freedom of such particles, *i.e.* the properties of their constituent atoms or molecules, are - to a certain extent - irrelevant to their description. Everyday examples of naturally occurring systems that are considered colloidal are blood (blood cells in a solvent) or milk (fat globules in a solvent). There is also a number of examples for chemically synthesized colloids, such as polystyrene or silica spheres.

Colloidal systems are highly intriguing, since they tend to exhibit some features known from atomic systems, such as crystallisation, and can therefore serve as model systems to study these features on more convenient time- and length scales: due to their relatively large size, they are easily observable with optical imaging techniques, such as confocal microscopy. Furthermore, the timescales on which phenomena like crystallisation take place are much longer than in atomic systems.

Many features known from atomic systems can be reproduced with simple colloidal models considering spherical particles with isotropic interactions. However, those simple models fail to describe many interesting phenomena seen in some naturally occurring colloidal systems such as proteins or virus capsids, which are known to self-organize into complex structures. This behaviour is driven by the fact that those systems exhibit spatially inhomogeneous surface charges, resulting in anisotropic interactions between those entities.

---

[1]from the Greek word $\kappa o \lambda \lambda \alpha$ - glue

Units with heterogeneously charged surfaces can be described with models for "patchy" colloids. The term "patchy" [1] refers to colloidal particles whose surfaces exhibit regions that interact in different ways than the rest of the surface. Those regions on the surface are referred to as "patches". The presence of patches lead to highly orientationally dependent interactions between two colloidal particles. Consequently, various anisotropic interactions scenarios can be modeled.

Apart from modeling naturally occurring self-assembly scenarios, patchy colloids can also be chemically synthesized, by modifying the surface of colloidal particles by physical or chemical methods in specific regions. This modification of the surface can be realized to yield very specific patterns, such that directional interactions can be controlled by modifying the surface decoration. Due to their anisotropic interactions, patchy colloids are promising candidates for a new generation of functionalised particles that could possibly act as building entities for larger, self-assembled structures, resulting in materials with particular properties and functions, depending on the tailored interactions of the participating particles. Recently, much progress has been made in the field of synthesis methods for those particles [2]; therefore, suitable theoretical models for predicting the physical properties of patchy colloids are of significant interest.

In this work, we investigate a special class of patchy colloids: negatively charged (spherical) colloids decorated on their poles with two patches carrying positive charges. Obviously, patches are mutually repulsive, as well as naked surface regions, while the interaction between patches and naked surface regions is attractive. The emerging interaction between two such particles can be either attractive or repulsive, depending on the relative orientation of the particles. Patchy colloids with these properties are called "inverse patchy colloids" [2] (IPCs) [3].

The aim of this thesis is to investigate the equilibrium phase diagram of these IPCs. To this end, we performed free energy calculations employing several methods:

(i) thermodynamic integration schemes that take advantage of reference systems of known free energy such as the ideal gas or the hard sphere system

---

[2]The term "patchy particles" was originally used for mutually attractive patches, thus the term "inverse" indicates mutually repulsive patches.

(ii) the *Einstein molecule approach* [4] for the calculation of reference structures in solid phases

(iii) direct coexistence methods [5] for estimations of the coexistence points by direct simulations of two phases in contact

With these methods, we were able to compute the free energy for four distinct phases - the fluid phase, two fcc structures and a solid structure composed of layers - and to evaluate their regions of thermodynamic stability.

Structure of the thesis

Chapter 2 introduces the coarse-grained model and the parameters used in the simulations for this thesis. Furthermore, we investigate the relation to the analytical description of the system.

Chapter 3 explains the theoretical tools necessary for the simulations performed for this thesis: thermodynamic integration from reference systems such as the ideal gas or the hard sphere fluid, the *Einstein Molecule Approach* for the calculation of free energies of solid phases, the direct coexistence method for obtaining coexistence points between two phases and Gibbs-Duhem integration for calculating coexistence lines between two phases in the phase diagram. Furthermore, some details on our simulation algorithm are given.

Chapter 4 presents the candidate structures used in the simulations for this thesis, as well as results obtained both from exploratory simulations and from simulations yielding actual coexistence points. Finally, a sketch of the phase diagram of the type of IPCs we studied is presented.

Chapter 5 summarizes the process in the course of which we have obtained our results as well as the results themselves and gives an outlook on possible future investigations involving the IPC system we studied.

All quantities in this thesis are expressed in reduced units (denoted with superscript *). Their definitions can be found in Appendix A.1.

2. The coarse-grained IPC model

The type of IPCs we are treating in this thesis was first introduced in reference [3]. These particles are positively charged spherical colloids decorated with two negatively charged patches placed symmetrically on the "poles" of the particle, while leaving the "equatorial" region uncovered (see figure 2.1). Experimentally, this setup can for instance be realized by letting two positively charged polyelectrolyte stars adsorb onto the surface of a negatively charged spherical colloid [6].

We describe the pair interaction between two IPCs within the coarse-grained approach introduced in [3]. In this approach, discrete charges are replaced by interaction spheres representing the interaction ranges of the central colloid and and the two patches, respectively. Within this description, the pair potential for a given distance of the IPCs and for given spatial orientations is evaluated by calculating the overlap volume between the respective interaction spheres, weighted by suitably chosen energy parameters (see subsection 2.2).

2.1. Parameters

Let us start by defining the characteristic parameters specifying the coarse-grained model (for details, see [3]). Figure 2.1 depicts a model IPC with its relevant parameters. In the coarse-grained (CG) model, the IPC consists of a central impenetrable hard sphere (index C in figure 2.1) with charge Z_c and radius $R_C = \sigma$ and a surrounding interaction sphere (index B in figure 2.1) of radius $R_B = \sigma + \frac{\delta}{2}$, δ is the interaction range. Spheres B and C are concentric (see figure 2.1). The patches, each carrying a charge Z_p, are represented by two spheres S^1 and S^2, located symmetrically along the central axis at a distance $e \leq \sigma$ (e for "eccentricity") The radii of the small spheres are equal: $R_{S^1} = R_{S^2} = \rho$. The size of the patches is

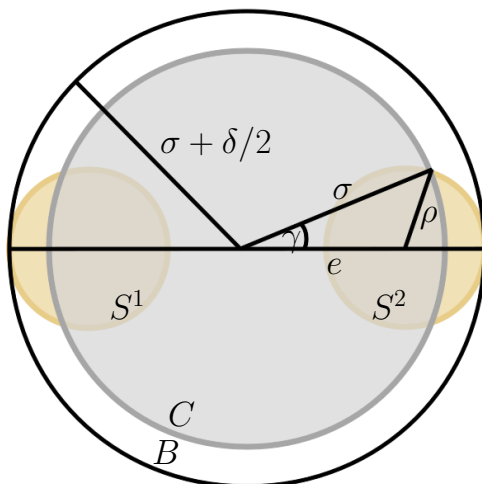characterized by the patch extension angle γ.

Figure 2.1.: Schematic depiction of the coarse-grained model for IPCs used in this thesis. For the description of the parameters, see text.

Of course, those parameters are not independent of each other. Based on the geometric relations shown in figure 2.1 and from the condition that each of the small spheres S^1 and S^2 touch the big sphere B from the inside, the relations between the parameters are as follows:

$$\delta = 2(e + \rho) - 2\sigma \tag{2.1}$$

$$\cos(\gamma) = \frac{\sigma^2 + e^2 + \rho^2}{2\sigma e} \tag{2.2}$$

with $\gamma < \frac{\pi}{2}$, since one patch can cover at most half of the surface of the colloid. Since the central colloidal particle is negatively charged, whereas the spherical patches carry a positive charge, different values for the charge differences $\Delta Z = Z_{\mathrm{c}} - 2Z_{\mathrm{p}}$ can be realized: The three charges can compensate, leading to an overall neutral particle ($\Delta Z = 0$); the charge of either the central colloid or the patches can prevail by a certain charge $\Delta Z \neq 0$ and lead to the cases of overcharged colloids or overcharged patches, respectively.

2.2. Pair potential

The effective interaction between two of those particles can either be attractive or repulsive, depending on their relative orientation. The design of the IPCs entails three basic reference interaction scenarios (see figure 2.2): equatorial-equatorial (EE) repulsion, equatorial-polar (EP) attraction and polar-polar (PP) repulsion. In the coarse-grained model it is assumed that the interaction potential of any other two-particle configuration is obtained as a superposition of the contributions obtained from those three different overlap situations. The EP configuration defines the energy minimum $\varepsilon_{\min}$ which is used to renormalize the potential function (see figure 2.3). The position vector $\boldsymbol{r}_i$ defines the spatial position of an IPCs,

Equatorial-Equatorial   Equatorial-Polar   Polar-Polar
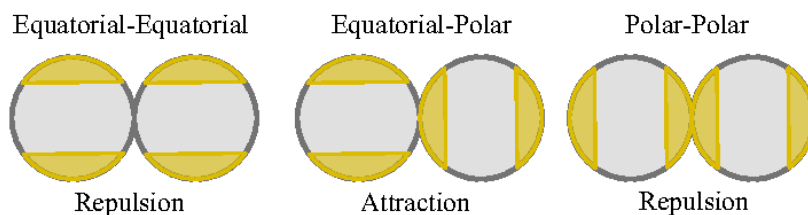
Repulsion   Attraction   Repulsion

Figure 2.2.: The three basic reference interaction scenarios of two IPCs: EE repulsion, EP attraction (energy minimum $\varepsilon_{\min}$) and PP repulsion

its orientation is given by the unit vector $\hat{\boldsymbol{n}}_i$ defining the axis connecting the two patches. Since the particles are axially symmetric, the vector $\hat{\boldsymbol{n}}_i$ is sufficient to describe the orientation. With $\boldsymbol{r}_{ij} = \boldsymbol{r}_j - \boldsymbol{r}_i$ being the vector between particles i and j, $r_{ij} = |\boldsymbol{r}_{ij}|$ their distance and defining the angles $\theta_i = \angle(\boldsymbol{r}_{ij}, \hat{\boldsymbol{n}}_i)$, $\theta_j = \angle(-\boldsymbol{r}_{ij}, \hat{\boldsymbol{n}}_j)$ and $\theta_{ij} = \angle(\hat{\boldsymbol{n}}_i, \hat{\boldsymbol{n}}_j)$, the interaction potential in the CG model for a pair of IPCs is given by

$$
V = \begin{cases} \infty & \text{if } r_{ij} < 2\sigma \\ U(r_{ij}, \theta_i, \theta_j, \theta_{ij}) & \text{if } 2\sigma \leq r_{ij} \leq 2\sigma + \delta \\ 0 & \text{if } 2\sigma + \delta < r_{ij} \end{cases} \qquad . \tag{2.3}
$$

$U(r_{ij}, \theta_i, \theta_j, \theta_{ij})$ is a sum of the contributions from BB-, BS- and SS-interactions. It is assumed that each of these contributions can be factorized into an energy strength ($\varepsilon_{\alpha\beta}$, with $\alpha, \beta = B, S$) and an orientational-geometric, dimensionless weight factor ($\omega_{\alpha\beta}$) which takes into account the distance and the relative orientation of the interacting particles [3]. The interaction potential thus reads:

$$U(r_{ij}, \theta_i, \theta_j, \theta_{ij}) = \omega_{BB}\varepsilon_{BB} + \omega_{BS}\varepsilon_{BS} + \omega_{SS}\varepsilon_{SS} . \tag{2.4}$$

The weight factors $\omega_{\alpha\beta}$ are proportional to the total overlap volume of all interaction spheres involved in the respective interaction:

$$\omega_{\alpha\beta} = \frac{\Omega_{OT}^{\alpha\beta}}{\Omega_R} \tag{2.5}$$

where $\Omega_R = \frac{4}{3}\pi\sigma^3$ is the normalizing reference volume guaranteeing dimensionless weight factors. In order to calculate the total overlap volumes (labeled with index 'OT'), all combinations of overlap volumes (labeled with index 'O') of big and small spheres have to be considered:

$$\Omega_{OT}^{BB} = \Omega_O^{B_i B_j} \tag{2.6}$$
$$\Omega_{OT}^{BS} = \Omega_O^{B_i S_j^1} + \Omega_O^{S_i S_j^2} + \Omega_O^{B_j S_i^1} + \Omega_O^{B_j S_i^2} \tag{2.7}$$
$$\Omega_{OT}^{SS} = \Omega_O^{S_i^1 S_j^1} + \Omega_O^{S_i^2 S_j^1} + \Omega_O^{S_i^1 S_j^2} + \Omega_O^{S_i^2 S_j^2} \tag{2.8}$$

where $i \neq j$ are the indices of the interacting particles and 1 and 2 indicate the respective patches.

2.3. Relation to the analytical description

The CG model described throughout the preceding sections and, more extensively, in reference [3] is a simplified model used in order to avoid the numerically cumbersome expressions obtained from the microscopic analytical description provided by the Debye-Hückel (DH) theory for dilute electrolytes [7]. The derivation of the effective pair interaction between two IPCs within this description can be found in reference [3]. Here, we shall only provide an idea of how the values of the fundamental parameters of the CG model are chosen in order to reproduce the features of the description provided by the Debye-Hückel theory, such as the symmetry of the system, the arrangement of the patches, the attractive/repulsive interaction, as well as the energy and length scales. As discussed in subsections 2.1 and 2.2, the CG model for IPCs depends on three parameters (one actually being a set of three parameters):

eccentricity e
The eccentricity e in the CG model is defined in figure 2.1 and the following equations. Its value is the same as in the DH description, which is a condition for guaranteeing the same geometrical setup. In the DH description, the eccentricity is defined as the distance between the centers of the respective charge distributions, which are represented by interaction spheres in the CG description, as explained above.

patch radius ρ
In the CG model, ρ depends on the choice of e and δ, as can be understood from equation (2.1). Since e is already fixed by the above condition, we are left with the interaction range δ, which needs to be chosen in order to reproduce the features of the analytical description. It is, in fact, related to the screening conditions of the electrolytic solution described within the DH theory. In the CG model, this relation is incorporated by assuming δ to be proportional to the Debye screening length κ^{-1} via $\delta = n\kappa^{-1}$ (with n being, for convenience, an integer number). δ is chosen to have the same value for all three types of interaction, BB, BS and SS. For given screening conditions (i.e. given κ^{-1}), n is chosen so that the interaction range δ reproduces the analytic potential of the DH description as accurate as possible. Since the derivation of the coarse-grained pair interaction between two

IPCs relies on high screening conditions ($k\sigma > 1$), as verified in reference [3], this fact has to be kept in mind when working with the CG model.

interaction strengths $\varepsilon_{BB}, \varepsilon_{BS}, \varepsilon_{BS}$

Like the above parameters, the energy strengths $\varepsilon_{BB}, \varepsilon_{BS}, \varepsilon_{BS}$ are obtained in an effort to reproduce the analytical pair potential of the DH description. The three reference configurations shown in figure 2.2 provide a starting point for those calculations. The radial pair potential in the coarse-grained model is obtained by considering each reference configuration (introduced above) separately, gradually increasing the distance between the two particles and evaluating the interaction energy analytically in each step. In an analogous way, the angular pair potential is found when rotating one particle with respect to the other, starting again from one of the reference configurations. Since the interaction energy which is evaluated in every step of the procedure is related to the interaction strengths $\varepsilon_{BB}, \varepsilon_{BS}, \varepsilon_{BS}$, their values can be adjusted to reproduce the analytical pair potential as accurate as possible. Table 2.1 lists the model parameters used in the simulations for this thesis. Figure 2.3 shows the radial and angular dependence both for the CG pair potential obtained from the mapping outlined above as well as the analytical results from the Debye-Hückel theory. The figures were created using the parameters from table 2.1. The potentials are depicted in units of the minimum pair energy $\varepsilon_{\min}$, which corresponds to the energy of the EP configuration (see figure 2.2).

Charge (overcharged colloid)	$\Delta Z = 30\ e$
Particle radius	$\sigma = 0.5$
Screening	$\kappa\ \sigma = 2$
Eccentricity	$e = 0.3\ \sigma$
Interaction range	$\delta = 0.25\ \sigma$
Patch radius	$\rho = 0.325\ \sigma$
Energy strengths	$\varepsilon_{BB} = 55.82\ \varepsilon_{\min}$
	$\varepsilon_{BS} = -315.27\ \varepsilon_{\min}$
	$\varepsilon_{SS} = 1281.08\ \varepsilon_{\min}$

Table 2.1.: Model parameters used in this thesis; e is the elementary charge, $\varepsilon_{\min}$ corresponds to the energy of the EP configuration (see figure 2.2);
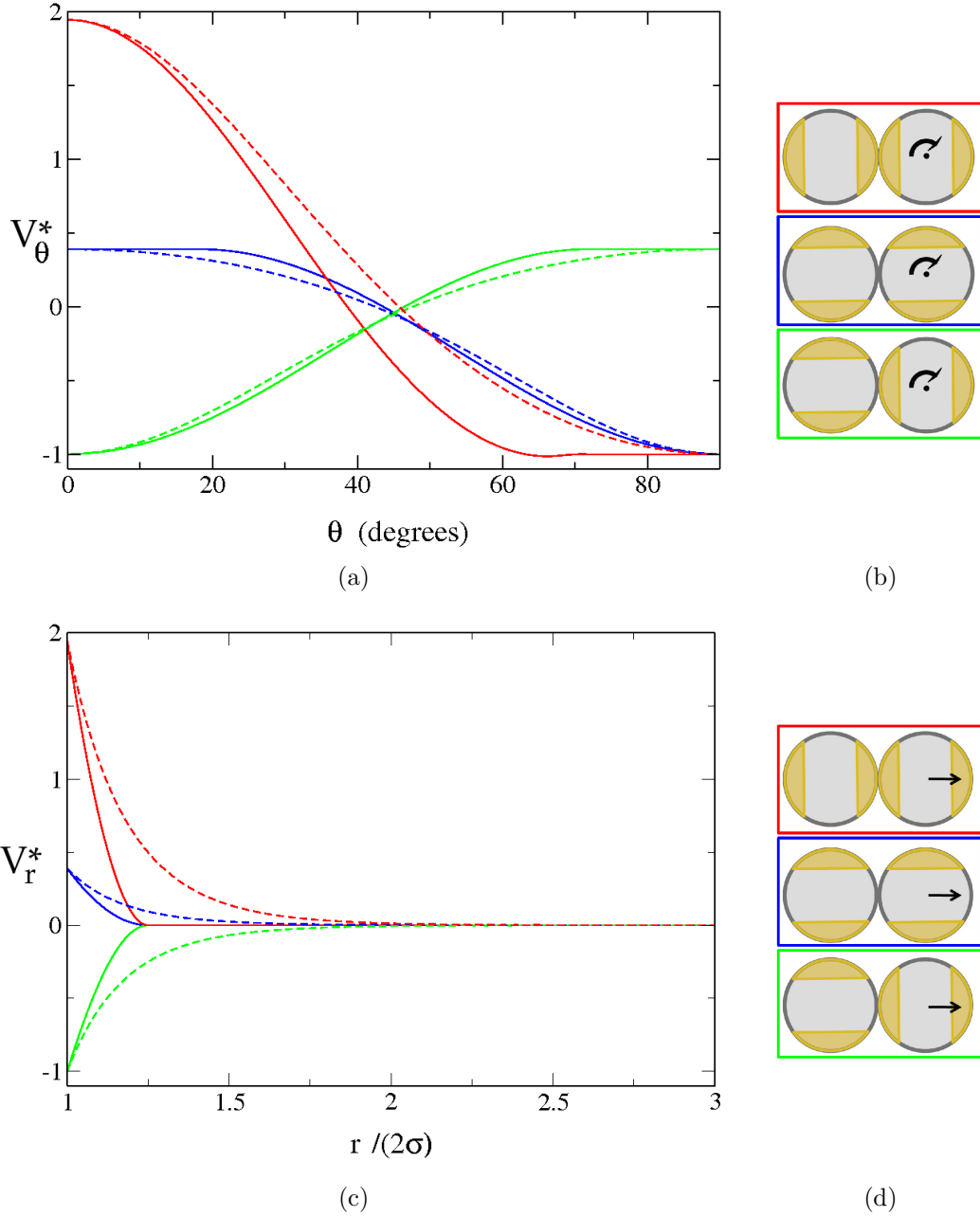
Figure 2.3.: (a): DH (dashed lines) and CG (continuous lines) results for the angular dependence of the IPC pair potential $V_\theta^* = \frac{V_\theta}{\varepsilon_{\min}}$ at fixed distance σ as a function of their relative angle θ (see arrow); for the three reference configurations, see panel (b)

(c): DH (dashed lines) an CG (continuous lines) results for the angular dependence of the IPC pair potential $V_r^* = \frac{V_r}{\varepsilon_{\min}}$ at fixed relative orientation as a function of their distance r; for the three reference configurations, see panel (d)

3. Method

When exploring the phase diagram of a given system with computer simulations, we are especially interested in the transition between two phases and in calculating the corresponding coexistence line.

A simplistic way to explore a phase transition is to perform simulations at different state points (e.g. different temperatures) and to analyze the behaviour of the system at hand. For example, one can prepare a crystalline structure and increase the temperature until the structure melts. This can be a reasonable approach for estimating the transition temperature between the crystal and the fluid phase.

However, when looking at first-order phase transitions, it has to be kept in mind that due to hysteresis effects the phase transition will very likely appear beyond the actual critical temperature. This is due to the fact that for a first-order phase transition to occur, a large free energy barrier has to be overcome. The height of this barrier is proportional to the interface area between the two phases. Therefore, when performing direct simulations of phase transitions, it is advisable to prepare the system in a way where the interface already exists (see section 3.3).

Much more accurate results are obtained when approaching the problem directly via calculating the free energies of the competing phases. Thermodynamic integration, combined with the Einstein crystal approach [4] for the solid case, are powerful tools for computing free energies of different phases.

However, before being able to evaluate the phase diagram with these tools, one needs a reliable estimate of the thermodynamic phases that are so-called *candidate structures* for the given system. While for simple models, candidate crystal structures can often be guessed based on symmetries of the model at hand or simply from experience, in the case of more complex models, several sophisticated

methods for obtaining those candidate structures at low temperatures have been introduced recently [8, 9, 10]. The work in this thesis relies on the optimisation technique described in reference [11], which is based on the ideas of evolutionary algorithms. With this technique, ordered equilibrium structures of the IPC model were identified at vanishing temperature. Working with these candidate structures at finite temperature, we have calculated the phase diagram with the tools and methods described in the following sections.

3.1. Thermodynamic Integration

3.1.1. Basic principles

In order to determine the relative stability of two phases, one has to identify the phase with lower free energy. Thermodynamic integration enables us to evaluate the free energy difference between a reference system and the system of interest. In the canonical ensemble (NVT ensemble), the corresponding thermodynamic potential is the Helmholtz free energy:

$$A = A(V, T) = U - TS \quad , \tag{3.1}$$

where U is the internal energy, T the temperature and S the entropy.
For the isothermal-isobaric ensemble (NpT ensemble), the thermodynamic potential is the Gibbs free energy:

$$G = G(P, T) = U - TS + pV \quad . \tag{3.2}$$

Besides the free energy, we will also frequently consider the chemical potential, which is defined in the following way:

$$\frac{\mu}{k_{\mathrm{B}}T} = \frac{G}{Nk_{\mathrm{B}}T} = \frac{A}{Nk_{\mathrm{B}}T} + \frac{pV}{Nk_{\mathrm{B}}T}$$
$$= \frac{A}{Nk_{\mathrm{B}}T} + \frac{p}{\rho k_{\mathrm{B}}T} \tag{3.3}$$

Unfortunately, the absolute values of thermodynamic potentials are difficult to access in computer simulations, since they are defined via the respective partition function (see definitions 3.5 and 3.20).

Often it is easier to obtain thermodynamic variables (e.g. pressure, energy), which are partial derivatives of the respective thermodynamic potential, directly from computer simulations. Integrating such a variable via a suitable integration path finally yields the respective thermodynamic potential. The integration path chosen has to be reversible, so no first-order transition must be encountered along the path. This can be ensured by checking the equation of state for discontinuities along the integration path. If no discontinuities occur throughout the density range covered by the integration path, thermodynamic integration is possible. If, however, the systems exhibits a first-order transition along the path, it might be advisable to use a thermodynamic integration scheme that follows a different path, or to combine several schemes in order to reach the state point of interest.

3.1.2. Thermodynamic integration in the canonical ensemble

Let $H = H(\boldsymbol{r}^N, \boldsymbol{p}^N)$ be the Hamiltonian function that describes the system; $\boldsymbol{r}^N = \{\vec{\boldsymbol{r}}_1 ... \vec{\boldsymbol{r}}_N\}$ and $\boldsymbol{r}^N = \{\vec{\boldsymbol{p}}_1 ... \vec{\boldsymbol{p}}_N\}$; Via the canonical partition function, given by

$$Z(N, V, T) = \frac{1}{N!} \frac{1}{h^{\mathrm{ND}}} \int d\boldsymbol{r}^N \ d\boldsymbol{p}^N \ e^{-\beta H(\boldsymbol{r}^N, \boldsymbol{p}^N)} \tag{3.4}$$

where $\beta = \frac{1}{k_{\mathrm{B}}T}$, we obtain the Helmholtz free energy A(N,V,T) as follows:

$$A = -k_B T \ln Z(N, V, T) \quad , \tag{3.5}$$

where k_B is the Boltzmann constant.

In order to access the value of the Helmholtz free energy $A(N, V, T)$ from simulations, its relation to ensemble averages of certain thermodynamic variables must be considered.

Integration along isochores

Let us define the internal energy U as the ensemble average (denoted by $\langle ... \rangle$) of the Hamiltonian of the system:

$$U = \left\langle H(\boldsymbol{r}^N, \boldsymbol{p}^N) \right\rangle \tag{3.6}$$

This average is evaluated as follows:

$$\langle H(\boldsymbol{r}^N, \boldsymbol{p}^N) \rangle = \frac{1}{Z} \frac{1}{N!} \frac{1}{h^{\mathrm{ND}}} \int d\boldsymbol{r}^N \, d\boldsymbol{p}^N \, H(\boldsymbol{r}^N, \boldsymbol{p}^N) \, e^{-\beta H(\boldsymbol{r}^N, \boldsymbol{p}^N)}$$

$$= -\frac{1}{Z} \frac{\partial Z}{\partial \beta} = -\frac{\partial}{\partial \beta} \ln Z \qquad (3.7)$$

With definition 3.5 of the Helmholtz free energy, we obtain:

$$U = \frac{\partial}{\partial \beta}(\beta A) \quad . \qquad (3.8)$$

Integrating this relation along an isochore (i.e., $V = const.$) from β_1 to β_2 yields:

$$\beta_2 A(V, \beta_2) - \beta_1 A(V, \beta_1) = \int_{\beta_1}^{\beta_2} U(V, \beta) \, d\beta \quad , \qquad (3.9)$$

which becomes, after a change in variable from $\beta = \frac{1}{k_{\mathrm{B}}T}$ to T ,

$$\frac{A(V, T_2)}{k_{\mathrm{B}}T_2} = \frac{A(V, T_1)}{k_{\mathrm{B}}T_1} - \int_{T_1}^{T_2} \frac{U(T)}{k_{\mathrm{B}}T^2} \, dT \quad . \qquad (3.10)$$

In simulations, the integrand in equation (3.10) can be evaluated in an NVT ensemble. $A(T_1, V)$ is here the known free energy of a reference system at temperature T_1.

Hamiltonian integration

The Hamiltonian $H(\boldsymbol{r}^N, \boldsymbol{p}^N)$ of a system has a potential energy contribution, $V(\boldsymbol{r}^N)$, and a kinetic energy contribution, $K(\boldsymbol{p}^N)$:

$$H(\boldsymbol{r}^N, \boldsymbol{p}^N) = V(\boldsymbol{r}^N) + K(\boldsymbol{p}^N) \quad . \qquad (3.11)$$

If two systems (labeled 1 and 2) at the same thermodynamic states have different interaction potentials, their Hamiltonians $H_1(\boldsymbol{r}^N, \boldsymbol{p}^N)$ and $H_2(\boldsymbol{r}^N, \boldsymbol{p}^N)$ differ in their potential energy contributions. In this case, we can evaluate the free energy difference between those two systems at the same thermodynamic state by Hamiltonian integration. To this end, we introduce a coupling parameter λ, ranging from 0 to 1, which couples the two Hamiltonians:

$$H(\boldsymbol{r}^N, \boldsymbol{p}^N; \lambda) = (1 - \lambda)H_1(\boldsymbol{r}^N, \boldsymbol{p}^N) + \lambda H_2(\boldsymbol{r}^N, \boldsymbol{p}^N) \quad . \qquad (3.12)$$

Considering the fact that the two Hamiltonians only differ in their potential energy contributions, this relation can be rewritten as:

$$H(\boldsymbol{r}^N, \boldsymbol{p}^N; \lambda) = (1 - \lambda)(V_1(\boldsymbol{r}^N) + K(\boldsymbol{p}^N)) + \lambda(V_2(\boldsymbol{r}^N) + K(\boldsymbol{p}^N))$$
$$= K(\boldsymbol{p}^N) + \underbrace{(1 - \lambda)V_1(\boldsymbol{r}^N) + \lambda V_2(\boldsymbol{r}^N)}_{V(\boldsymbol{r}^N; \lambda)} \tag{3.13}$$

In the expression for the canonical partition function 3.4, we can thus evaluate the integrals over momentum space:

$$Z(N, V, T; \lambda) = \frac{1}{\Lambda^{3N} N!} \int e^{\beta V(\boldsymbol{r}^N, \lambda)} \, d\boldsymbol{r}^N \quad , \tag{3.14}$$

where $V(\boldsymbol{r}^N; \lambda)$ is defined in equation (3.13). The thermal de Broglie wavelength in equation (3.14), which is defined as

$$\Lambda = \frac{h}{\sqrt{2\pi m k_{\mathrm{B}} T}} \quad , \tag{3.15}$$

stems from the integration over momentum space.

We reconsider the definition of the Helmholtz free energy (3.5), which depends now in addition on the coupling parameter λ. Taking the derivative of $A(N, V, T; \lambda)$ with respect to λ yields:

$$\left(\frac{\partial A(N, V, T; \lambda)}{\partial \lambda} \right)_{N,V,T} = -\frac{1}{\beta} \frac{\partial}{\partial \lambda} \ln Z(N, V, T; \lambda)$$
$$= -\frac{1}{\beta} \frac{1}{Z(N, V, T; \lambda)} \frac{\partial Z(N, V, T; \lambda)}{\partial \lambda}$$
$$= \frac{\int d\boldsymbol{r}^N e^{-\beta V(\boldsymbol{r}^N, \lambda)} \frac{\partial}{\partial \lambda} V(\boldsymbol{r}^N, \lambda)}{\int d\boldsymbol{r}^N e^{-\beta V(\boldsymbol{r}^N, \lambda)}}$$
$$= \left\langle \frac{\partial V(\boldsymbol{r}^N, \lambda)}{\partial \lambda} \right\rangle_{N,V,T} \quad . \tag{3.16}$$

With the definition of $V(\boldsymbol{r}^N, \lambda)$ in equation (3.13), we can rewrite this relation as:

$$\left(\frac{\partial A(N, V, T; \lambda)}{\partial \lambda} \right)_{N,V,T} = \left\langle V_2(\boldsymbol{r}^N) - V_1(\boldsymbol{r}^N) \right\rangle_{N,V,T} \quad . \tag{3.17}$$

We have now expressed the derivative of the free energy with respect to the coupling parameter λ as an ensemble average of the difference in the potential energy of systems 1 and 2.

Integrating (3.17) with respect to λ yields:

$$A_2(V,T,N;\lambda=1) = A_1(V,T,N;\lambda=0) + \int_{\lambda=0}^{\lambda=1} \langle V_2(\boldsymbol{r}^N) - V_1(\boldsymbol{r}^N) \rangle_{N,V,T} \, d\lambda \quad . \tag{3.18}$$

If the free energy $A_1(V,T,N;\lambda=0)$ of system 1 is known, the free energy of system 2, $A_2(V,T,N;\lambda=1)$, is obtained by evaluating the integral in equation 3.18 numerically. The integrand can be obtained from NVT simulations for different values of λ. We simulate the system with the Hamiltonian defined in (3.13) and evaluate the term $V_2(\boldsymbol{r}^N) - V_1(\boldsymbol{r}^N)$ regularly. At the end of the simulation, we compute the average $\langle V_2(\boldsymbol{r}^N) - V_1(\boldsymbol{r}^N) \rangle$.

3.1.3. Thermodynamic integration in the isothermal-isobaric ensemble

The partition function of the isothermal-isobaric ensemble, which we shall call $Q(N,p,T)$, reads:

$$Q(N,p,T) = \frac{1}{N!} \frac{1}{h^{\mathrm{ND}}} \int dV \int d\boldsymbol{r}^N \, d\boldsymbol{p}^N \; e^{-\beta H(\boldsymbol{r}^N,\boldsymbol{p}^N)} e^{-\beta p V} \tag{3.19}$$

Via this expression, the Gibbs free energy $G(N,p,T)$ is given by:

$$G(N,p,T) = -k_{\mathrm{B}} T \ln Q(N,p,T) \quad . \tag{3.20}$$

In order to obtain $G(N,p,T)$ from our simulations, we must relate it to ensemble averages of suitable thermodynamic variables.

Integration at $\beta p = $ const.

The ensemble average of the Hamiltonian $H(\boldsymbol{r}^N, \boldsymbol{p}^N)$ in the NpT ensemble is obtained in the following way:

$$
\begin{aligned}
\langle H(\boldsymbol{r}^N, \boldsymbol{p}^N) \rangle &= \frac{1}{N!} \frac{1}{h^{ND}} \frac{1}{Q(N,p,T)} \int_0^\infty dV \int d\boldsymbol{r}^N \; d\boldsymbol{p}^N \; H(\boldsymbol{r}^N, \boldsymbol{p}^N) e^{-\beta H(\boldsymbol{r}^N, \boldsymbol{p}^N)} e^{-\beta pV} \\
&= -\frac{1}{Q(N,p,T)} \left(\frac{\partial}{\partial \beta} Q(N,p,T) \right)_{\beta p = \text{const.}} \\
&= -\left(\frac{\partial}{\partial \beta} \ln Q(N,p,T) \right)_{\beta p = \text{const.}}
\end{aligned}
\tag{3.21}
$$

With definition 3.20 of the Gibbs free energy $G(N,p,T)$ and with the internal energy $U = \langle H(\boldsymbol{r}^N, \boldsymbol{p}^N) \rangle$ we obtain:

$$
U = \left(\frac{\partial}{\partial \beta} \beta G \right)_{\beta p = \text{const.}} \qquad .
\tag{3.22}
$$

Integrating this relation along a path with $\beta p = $ const. from β_1 to β_2 yields:

$$
\beta_2 G(\beta_2, p(\beta_2)) - \beta_1 G(\beta_1, p(\beta_1)) = \int_{\beta_1}^{\beta_2} U(\beta, p(\beta)) \; d\beta \quad ,
\tag{3.23}
$$

with $p(\beta) = \frac{\text{const.}}{\beta}$. Dividing by the number of particles, yields (via $\mu = \frac{G}{N}$ with μ being the chemical potential)

$$
\beta_2 \mu(\beta_2, p(\beta_2)) = \beta_1 \mu(\beta_1, p(\beta_1)) + \int_{\beta_1}^{\beta_2} u(\beta, p(\beta)) \; d\beta \;,
\tag{3.24}
$$

where u is the internal energy per particle. The integrand in equation (3.24) is evaluated in NpT simulations at several temperatures along the integration path $\beta p = $ const. .

The term $\beta_1 \mu(\beta_1, p(\beta_1))$ stems, again, from the reference system. At hight temperatures, the IPC model behaves a lot like the hard sphere system, so if β_1 corresponds to a high temperature, we can identify the reference term with the chemical potential of the hard sphere system at high temperatures. In order to account for the internal energy of the IPC model, we add a corresponding contribution to the reference term, which is however relatively small at high temperatures and the

respective pressures. With μ_{HS} being the chemical potential of the hard sphere system, the reference term reads:

$$\beta_1 \mu(\beta_1, p_1) = \beta_1 \mu_{\text{HS}}(p_1) + \beta_1 u. \tag{3.25}$$

Integration along isotherms

From the fundamental thermodynamic relation

$$dU = TdS - pdV \tag{3.26}$$

and with the definition (3.1) of the Helmholtz free energy, we obtain the following relation:

$$\begin{aligned} dA &= d(U - TS) \\ &= TdS - pdV - d(TS) \\ &= TdS - pdV - TdS - SdT \\ &= -pdV - SdT \end{aligned} \tag{3.27}$$

and therefore,

$$-p = \left(\frac{\partial A}{\partial V}\right)_{NT}. \tag{3.28}$$

Thus, in order to obtain the Helmholtz free energy $A(V, T)$, we can integrate this relation along an isotherm:

$$A(V_2, T) - A(V_1, T) = -\int_{V_1}^{V_2} p(V, T)\, dV. \tag{3.29}$$

The straightforward way to evaluate the integral in equation (3.29) with computer simulations is to perform NVT simulations at different volumes and evaluating the pressure via the virial expression. However, in the case of discontinuous potentials as the IPC coarse-grained potential, the virial is not easily accessible.

Therefore, we switch to NpT simulations, which we perform at different pressures p and at fixed temperature T. In each simulation, we evaluate the total number density, which is defined as $\rho = \frac{N}{\langle V \rangle}$ via the average volume $\langle V \rangle$ of the system. Thus, we can rewrite the integral in equation (3.29) as:

$$A(\rho_2, T) = A(\rho_1, T) + \int_{\rho_1}^{\rho_2} \frac{Np(\rho, T)}{\rho^2}\, d\rho \tag{3.30}$$

$A(\rho_1, T)$ is the free energy of a reference system - a thermodynamic state for which the free energy is known.

3.1.4. Reference states for free energy calculations

As we have seen above, the integration from a reference state to any other thermodynamic state is quite straightforward as long as no first-order phase transition is crossed along the integration path. If there exists a reference state with known free energy, a thermodynamic integration scheme that fits the problem can be applied to obtain the free energy of the state of interest.

For fluid phases, the ideal gas or the hard sphere fluid are ideal candidates for the reference states. The solid phase of the hard sphere model can also act as a reference for some solids, for instance with FCC structure (see subsection 4.3.2). For most solids, however, the reference state has to be computed with a separate method before integrating to different state points.

In the simulations performed for this thesis, the evaluation of the thermodynamic properties of the solid reference states was carried out following a method that is a special variant of the *Einstein crystal method* described in reference [4], where this variant is labeled *Einstein molecule approach*.

3.2. The Einstein Molecule Approach

In order to obtain a thermodynamic potential, e.g. the Helmholtz free energy $A(\rho, T)$ for a solid phase of a given system, the ultimate goal is to be able to perform thermodynamic integration following the concepts described in subsection 3.1. As was shown above, if the Helmholtz free energy $A(\rho, T)$ is known at a certain reference state point, we can integrate to any other thermodynamic state point using thermodynamic integration.

For most solid phases, this reference free energy can not be taken directly from a single reference system, such as to the ideal gas or the hard sphere system as in the case of the fluid phase. However, we can use the *Einstein molecule approach* [4] to

explicitly compute the free energy of the system of interest at a state point (e.g. (ρ_1, T_1)) and use this state point as a reference for thermodynamic integration to any other state point (ρ_2, T_2). The method was originally introduced by Frenkel and Ladd [12] in 1984 and has become a standard method for evaluating the free energy of solids.

The ideal Einstein crystal is used as a starting point for the computation. It is an ideal crystal (i.e. without interactions between the particles) in which the particles are linked to their lattice sites by harmonic springs. The free energy of this model system can be evaluated in a straightforward way, as is shown later in this section. However, there is no direct path that links the thermodynamic properties of the Einstein crystal to those of the solid of interest. Several "intermediate" systems have to be considered when constructing this path. In order to obtain the free energy of the solid, the *differences* in free energy between these intermediate systems have to be computed step by step.

The systems under consideration are:

1. Ideal Einstein crystal with one fixed particle (denoted by indices $_{\mathrm{E}}^{\text{fix-id}}$)

2. Interacting Einstein crystal with one fixed particle (denoted by indices $_{\mathrm{E}}^{\text{fix-int}}$)

3. Solid with one fixed particle (denoted by indices $_{\text{sol}}^{\text{fix}}$)

4. Unconstrained solid (denoted by indices $_{\text{sol}}$)

In the *Einstein molecule* approach we define one particle as a reference point ("carrier") for the whole crystal. A translation of this particle implies a corresponding translation of the whole crystal. Hence, the carrier particle is not bound harmonically to its lattice position, but rather acts as a reference point for all the other particles. If the carrier particle is fixed, as is the case in systems 1., 2. and 3. (see definitions above), this implies that the crystal is not allowed to move. This restriction has a numerical background for which the reader is referred to R. [4]. In the original method (the *Einstein crystal* method [12]), translations of the whole crystal are prevented by keeping the center of mass of the system fixed.

We can now write the free energy of the solid of interest, A_{sol}, as a sum of the free

energy differences between systems 1. and 2., 2. and 3. and 3. and 4.:

$$A_{\text{sol}} = A_{\text{E}}^{\text{fix-id}} + \underbrace{\left(A_{\text{E}}^{\text{fix-int}} - A_{\text{E}}^{\text{fix-id}}\right)}_{\Delta A_1 \ (1. \rightarrow 2.)} + \underbrace{\left(A_{\text{sol}}^{\text{fix}} - A_{\text{E}}^{\text{fix-int}}\right)}_{\Delta A_2 \ (2. \rightarrow 3.)} + \underbrace{\left(A_{\text{sol}} - A_{\text{sol}}^{\text{fix}}\right)}_{\Delta A_3 \ (3. \rightarrow 4.)} \tag{3.31}$$

or, with the convenient choice $A_0 = A_{\text{E}}^{\text{fix-id}} + \Delta A_3$:

$$A_{\text{sol}} = A_0 + \Delta A_1 + \Delta A_2 \quad . \tag{3.32}$$

Each of the contributions in equation (3.32) has to be evaluated separately. The process of how to obtain the three contributions is described in the following. The derivations presented in this section retrace the ones found in R. [4].

3.2.1. Evaluation of A_0

A_0 is a sum of the free energy of the Einstein crystal with fixed carrier particle, $A_{\text{E}}^{\text{fix-id}}$, and the free energy difference between systems 3. and 4., ΔA_3. In the following, the evaluation of these terms is explained:

- $A_{\text{E}}^{\text{fix-id}}$: Let us start be deriving the free energy for the ideal (unconstrained) Einstein crystal A_E^{id} and then proceed to the case where one particle is kept fixed to its lattice position. The Hamiltonian of the ideal Einstein crystal

$$H_{\text{E}}^{\text{id}} = H_{\text{E}}^{\text{id}}(\boldsymbol{p}^N, \boldsymbol{r}'^N, \psi^N) = K_{\text{E}}^{\text{id}}(\boldsymbol{p}^N) + V_{\text{E}}^{\text{id}}(\boldsymbol{r}'^N, \psi^N) \quad , \tag{3.33}$$

  has a kinetic energy contribution

$$K_{\text{E}}^{\text{id}}(\boldsymbol{p}^N) = \sum_{i=1}^{N} \frac{\boldsymbol{p}_i^2}{2m} \tag{3.34}$$

  and two contributions to the potential energy

$$V_{\text{E}}^{\text{id}}(\boldsymbol{r}'^N, \psi^N) = V_{\text{E,or}}^{\text{id}}(\psi_1^N) + V_{\text{E,trans}}^{\text{id}}(\boldsymbol{r}'^N) \quad . \tag{3.35}$$

  In those relations, the $\boldsymbol{p}^N$ are the momenta of the particles, $\boldsymbol{r}'^N$ are their positions relative to their equilibrium positions (see below) and ψ^N are the angles with their equilibrium orientations (see below). The orientational contribution is given by

$$V_{\text{E,or}}^{\text{id}} = \sum_{i=1}^{N} v_{\text{E,or}}^{\text{id}} = \Lambda_{\text{E}} \sum_{i=1}^{N} \sin^2(\psi_i) \quad , \tag{3.36}$$

with ψ_i being the angle between the actual orientation of particle i and its equilibrium orientation in the reference Einstein lattice. The corresponding forces urge the particles' spatial orientations towards their equilibrium orientations. In systems that are characterized by a more complex geometry than the IPC system, one angle is not sufficient to describe this orientational dependence in the potential energy - then, equation (3.36) becomes a more complicated relation [4]. Λ_E is the coupling constant, parameterizing the strength of the coupling to the equilibrium orientation.

The translational contribution in equation (3.35) is given by

$$V_{E,\text{trans}}^{\text{id}} = \sum_{i=2}^{N} v_{E,\text{trans}}^{\text{id}} = \Lambda_E \sum_{i=2}^{N} (\boldsymbol{r}_i - \boldsymbol{r}_{i0})^2 \quad , \tag{3.37}$$

with the $\boldsymbol{r}_i$, $i = 1, ..., N$ being the current positions of the particles, while the $\boldsymbol{r}_{i0}$, $i = 1, ..., N$ denoting their equilibrium position. This potential energy keeps the particles harmonically bonded to their lattice sites. Λ_E is the coupling parameter of the springs which is chosen to be the same as the coupling of the orientational part (this choice is convenient, but not compulsory). Note that the sum in equation (3.37) starts from particle 2, because the carrier particle (specified by index 1) is not harmonically bonded to its position, but can move freely in space.

With the above definitions and with the relative variables $\boldsymbol{r}_i' = \boldsymbol{r}_i - \boldsymbol{r}_1$, $i = 1, ..., N$ we can write the canonical partition function of the ideal Einstein crystal as:

$$Z_E^{\text{id}} = \frac{1}{\Lambda^{3N}} \underbrace{\int d\boldsymbol{r}_1}_{V} \underbrace{\int e^{-\beta\left[V_{E,\text{trans}}^{\text{id}}(\boldsymbol{r}'^N) + V_{E,\text{or}}^{\text{id}}(\psi^N)\right]} d\psi_1 \, d\boldsymbol{r}_2' \, d\psi_2 \, ... \, d\boldsymbol{r}_N' \, d\psi_N}_{\kappa}$$

$$\tag{3.38}$$

where - in the unconstrained case - the first integral is equal to the volume of the simulation box, since the carrier particle (i.e. the particle with index 1) can assume any position in the entire volume (and thereby translate the whole crystal). Λ denotes the thermal de Broglie wavelength (see equation (3.15)) and originates from the fact that integration over momenta was already carried out in equation (3.38).

Hence, the canonical partition function of the ideal Einstein crystal can be written as:

$$Z_{\mathrm{E}}^{\mathrm{id}} = \frac{V}{\Lambda^{3N}} \kappa \quad , \tag{3.39}$$

leaving κ as the only term that has to be evaluated. κ factorizes into an orientational and a translational contribution:

$$\kappa = \underbrace{\int e^{-\beta v_{\mathrm{E,or}}^{\mathrm{id}}(\psi_i)} \, d\psi_1 \, ... \, d\psi_N}_{\kappa_{\mathrm{or}}} \underbrace{\int e^{-\beta v_{\mathrm{E,trans}}^{\mathrm{id}}(r_i')} \, d\boldsymbol{r}_2' \, ... \, d\boldsymbol{r}_N'}_{\kappa_{\mathrm{trans}}} \tag{3.40}$$

The integral over the orientational part reads:

$$\kappa_{\mathrm{or}} = \left(\frac{1}{8\pi^2} \int e^{-\beta v_{\mathrm{E,or}}^{\mathrm{id}}(\theta,\phi,\gamma)} \sin\theta \, d\phi \, d\theta \, d\gamma \right)^N \tag{3.41}$$

where θ, ϕ and γ are the Euler angles describing the particles' orientations in space. Note that we have changed the integration variable from ψ in equation (3.40) to θ, ϕ and γ in equation (3.41). For the relation between ψ and the Euler angles θ, ϕ and γ, see Appendix A.2. The integral given in equation (3.41) has to be evaluated numerically, for example using Monte Carlo integration.

The translational contribution to the term κ in equation (3.40) reads:

$$\kappa_{\mathrm{trans}} = \int e^{-\beta \Lambda_{\mathrm{E}} \sum_{i=2}^{N} (r_i')^2} \, d\boldsymbol{r}_2' \, ... \, d\boldsymbol{r}_N' \quad , \tag{3.42}$$

it is a product of Gaussian integrals. The result for κ_{t} reads:

$$\kappa_{\mathrm{trans}} = \left(\sqrt{\frac{\pi}{\beta \Lambda_{\mathrm{E}}}} \right)^{3(N-1)} . \tag{3.43}$$

The partition function for the ideal Einstein crystal that we considered in equation (3.39) thus becomes:

$$Z_{\mathrm{E}}^{\mathrm{id}} = \frac{V}{\Lambda^{3N}} \left(\sqrt{\frac{\pi}{\beta \Lambda_{\mathrm{E}}}} \right)^{3(N-1)} \kappa_{\mathrm{or}} \tag{3.44}$$

Hence, we obtain for the Helmholtz free energy of the ideal Einstein crystal:

$$\frac{1}{N}\frac{A_E^{id}}{k_B T} = -\frac{1}{N}\ln Z_E^{id}$$
$$= \frac{1}{N}\ln\left(\frac{\Lambda^3}{V}\right) + \frac{3}{2}\left(1 - \frac{1}{N}\right)\ln\left(\frac{\Lambda^2\beta\Lambda_E}{\pi}\right) - \frac{1}{N}\ln(\kappa_{or}) . \quad (3.45)$$

- $A_E^{\text{fix-id}}$: We now consider the changes we have to make when adapting equation (3.45) to the case of a carrier particle with fixed position. In that case, the integral over $\boldsymbol{r}_1$ in the partition function (3.38) equals 1, since in that case the integrand is a delta distribution determining the position of the particle. Furthermore, this particle does not provide a momentum contribution to the Hamiltonian, hence the integral over momentum space in the partition function 3.38 extends only over 3(N-1) momentum components. Consequently, Λ^{3N} has to be replaced by $\Lambda^{3(N-1)}$ in the partition function, which now reads:

$$Z_E^{\text{fix-id}} = \frac{1}{\Lambda^{3(N-1)}}\,\kappa \quad (3.46)$$

Thus, the expression for the free energy of the Einstein crystal with fixed carrier particle is given by:

$$\frac{1}{N}\frac{A_E^{\text{fix-id}}}{k_B T} = \frac{3}{2}\left(1 - \frac{1}{N}\right)\ln\left(\frac{\Lambda^2\beta\Lambda_E}{\pi}\right) - \frac{1}{N}\ln(\kappa_{or}) \quad (3.47)$$

- ΔA_3: We now compute the difference in free energy between the solid with a fixed carrier molecule and the unconstrained solid. This difference can be written in the following way:

$$\Delta A_3 = A_{sol} - A_{sol}^{\text{fix}}$$
$$= -k_B T\,\ln\frac{Z_{sol}}{Z_{sol}^{\text{fix}}} = k_B T\,\ln\frac{Z_{sol}^{\text{fix}}}{Z_{sol}} \quad , \quad (3.48)$$

with Z_{sol} and Z_{sol}^{fix} being the respective partition functions, which we want to write down explicitly in the following.

For the solid with fixed carrier particle, the partition function reads:

$$Z_{\text{sol}}^{\text{fix}} = \frac{1}{(N-1)!} \frac{1}{\Lambda^{3(N-1)}} \underbrace{\int e^{-\beta U_{\text{sol}}(\boldsymbol{R}_1, \omega_1, \boldsymbol{r}_2, \omega_2, ..., \boldsymbol{r}_{\text{N}}, \omega_{\text{N}})} \, d\omega_1 d\boldsymbol{r}_2 d\omega_2 ... d\boldsymbol{r}_{\text{N}} d\omega_{\text{N}}}_{=\eta} \quad ,$$

(3.49)

where the term $\frac{1}{(N-1)!}$ stems from the fact that we have $N-1$ indistinguishable particles - particle 1 is distinguished because of its fixed position, which is $\boldsymbol{R}_1$. Like in the derivations above, in the case of one fixed particle, the integrals over momentum space give $\Lambda^{-3(N-1)}$.

Note that the integral η in equation (3.49), is, in fact, independent of the choice of $\boldsymbol{R}_1$. We can show this by rewriting the internal energy U_{sol} appearing in the integrand in equation (3.49) in the following way:

$$U_{\text{sol}}(\boldsymbol{R}_1, \omega_1, \boldsymbol{r}_2, \omega_2, ..., \boldsymbol{r}_{\text{N}}, \omega_{\text{N}}) = U_{\text{sol}}(\boldsymbol{0}, \omega_1, \boldsymbol{r}_2 - \boldsymbol{R}_1, \omega_2, ..., \boldsymbol{r}_{\text{N}} - \boldsymbol{R}_1, \omega_{\text{N}}) \quad .$$

(3.50)

This is allowed since the internal energy of the solid is invariant under translations of the whole solid. If we now define relative coordinates, such that $\boldsymbol{r}_i' = \boldsymbol{r}_i - \boldsymbol{R}_1$, the partition function (3.49) reads:

$$Z_{\text{sol}}^{\text{fix}} = \frac{1}{(N-1)!} \frac{1}{\Lambda^{3(N-1)}} \int e^{-\beta U_{\text{sol}}(\boldsymbol{0}, \omega_1, \boldsymbol{r}_2', \omega_2, ..., \boldsymbol{r}_{\text{N}}', \omega_{\text{N}})} \, d\omega_1 d\boldsymbol{r}_2' d\omega_2 ... d\boldsymbol{r}_{\text{N}}' d\omega_{\text{N}} \quad .$$

(3.51)

From the above relation, it is obvious that η (see equation (3.49)) can not depend on the value of $\boldsymbol{R}_1$. This result is not unexpected, since a dependence on $\boldsymbol{R}_1$ would also imply a dependence of the partition function on that value.

The partition function of the unconstrained solid has the following form:

$$\begin{aligned} Z_{\text{sol}} &= \frac{1}{N!} \frac{1}{\Lambda^{3N}} \int e^{-\beta U_{\text{sol}}(\boldsymbol{r}_1, \omega_1, \boldsymbol{r}_2, \omega_2, ..., \boldsymbol{r}_{\text{N}}, \omega_{\text{N}})} \, d\boldsymbol{r}_1 d\omega_1 d\boldsymbol{r}_2 d\omega_2 ... d\boldsymbol{r}_{\text{N}} d\omega_{\text{N}} \\ &= \frac{1}{N!} \frac{1}{\Lambda^{3N}} \int_V \underbrace{\int e^{-\beta U_{\text{sol}}(r_1, \omega_1, r_2, \omega_2, ..., r_{\text{N}}, \omega_{\text{N}})} \, d\omega_1 d\boldsymbol{r}_2 d\omega_2 ... d\boldsymbol{r}_{\text{N}} d\omega_{\text{N}}}_{=\eta} \, d\boldsymbol{r}_1 \quad . \end{aligned}$$

(3.52)

In the above relation, the same argument as above holds for the inner integral η, which does not depend on the position $\boldsymbol{r}_1$ of the first particle. Particularly, the values of η are the same in equations (3.49) and (3.52).

Since η does not depend on $\boldsymbol{r}_1$, the integral over $\boldsymbol{r}_1$ simply yields the simulation volume V. We can now write the free energy difference from equation (3.48) as:

$$\Delta A_3 = k_{\mathrm{B}}T \ \ln \frac{Z_{\mathrm{sol}}^{\mathrm{fix}}}{Z_{\mathrm{sol}}}$$

$$= k_{\mathrm{B}}T \ \ln \left(\frac{1}{(N-1)!} \frac{1}{\Lambda^{3(N-1)}} \eta \left(\frac{1}{N!} \frac{1}{\Lambda^{3N}} V \eta \right)^{-1} \right)$$

$$= k_{\mathrm{B}}T \ \ln \left(\frac{N!}{(N-1)!} \frac{\Lambda^{3N}}{\Lambda^{3(N-1)}} \frac{1}{V} \right)$$

$$= k_{\mathrm{B}}T \left(\ln(N) + \ln \left(\frac{\Lambda^3}{V} \right) \right) \quad . \tag{3.53}$$

We thus obtain as our **first contribution** to the free energy of the solid (defined in equation (3.32)):

$$\frac{A_0}{Nk_BT} = \frac{1}{N}\ln(N) + \frac{1}{N}\ln\left(\frac{\Lambda^3}{V}\right) + \frac{3}{2}\left(1 - \frac{1}{N}\right)\ln\left(\frac{\Lambda^2 \beta \Lambda_{\mathrm{E}}}{\pi}\right) - \frac{1}{N}\ln(\kappa_{\mathrm{or}}) \tag{3.54}$$

3.2.2. Evaluation of ΔA_1

In the next step, the change in free energy when going from the ideal Einstein crystal to the interacting Einstein crystal (both with fixed carrier particle) is computed.

In order to evaluate this term, we first consider two arbitrary systems (labeled 1 and 2) with different Hamiltonians $H_1(\boldsymbol{r}^N, \boldsymbol{p}^N)$ and $H_2(\boldsymbol{r}^N, \boldsymbol{p}^N)$ and, consequently, two different canonical partition functions Z_1 and Z_2 (as defined equation (3.4)). Their free energy difference ΔA is given by:

$$\Delta A = A_2 - A_1 = -k_B T \ln Z_2(N, V, T) + k_B T \ln Z_1(N, V, T)$$

$$= -k_B T \ln \frac{\int e^{-\beta H_2(\boldsymbol{r}^N, \boldsymbol{p}^N)} \, d\boldsymbol{r}^N \, d\boldsymbol{p}^N}{\int e^{-\beta H_1(\boldsymbol{r}^N, \boldsymbol{p}^N)} \, d\boldsymbol{r}^N \, d\boldsymbol{p}^N} \quad . \tag{3.55}$$

Multiplying the integrand in the nominator by $e^{-\beta H_1(\boldsymbol{r}^N, \boldsymbol{p}^N)} \, e^{\beta H_1(\boldsymbol{r}^N, \boldsymbol{p}^N)} = 1$ yields

$$A_2 - A_1 = -k_B T \ln \frac{\int e^{-\beta(H_2(\boldsymbol{r}^N, \boldsymbol{p}^N) - H_1)} e^{-\beta H_1(\boldsymbol{r}^N, \boldsymbol{p}^N)} \, d\boldsymbol{r}^N \, d\boldsymbol{p}^N}{\int e^{-\beta H_1} \, d\boldsymbol{r}^N \, d\boldsymbol{p}^N}$$

$$= -k_B T \ln \langle e^{-\beta(H_2(\boldsymbol{r}^N, \boldsymbol{p}^N) - H_1(\boldsymbol{r}^N, \boldsymbol{p}^N))} \rangle_1 \quad, \tag{3.56}$$

where $\langle e^{-\beta(H_2(\boldsymbol{r}^N, \boldsymbol{p}^N) - H_1(\boldsymbol{r}^N, \boldsymbol{p}^N))} \rangle_1$ is the ensemble average of the term $e^{-\beta(H_2 - H_1)}$ taken in system 1.

Since we want to calculate the difference in free energy between the ideal Einstein crystal and the interacting Einstein crystal, we proceed with the following assignments (the indices are explained in the introduction to this chapter):

$$A_1 = A_E^{\text{fix-id}}$$
$$A_2 = A_E^{\text{fix-int}}$$
$$H_1 = H_E^{\text{id}}(\boldsymbol{r}'^N, \boldsymbol{p}^N, \psi^N)$$
$$H_2 = H_E^{\text{int}} = H_E^{\text{id}}(\boldsymbol{r}'^N, \boldsymbol{p}^N, \psi^N) + V_{\text{sol}}(\boldsymbol{r}^N) \quad.$$

The Hamiltonian of the interacting Einstein crystal H_E^{int} is equal to the Hamiltonian of the ideal Einstein crystal H_E^{id} plus an additional term V_{sol} accounting for the interparticle potential energy of the solid (for the dependences, see above).

Entering these values in equation (3.56) for the free energy difference of two arbitrary systems we obtain - as the **second contribution** to the free energy of the solid, (3.32) -

$$\Delta A_1 = -k_B T \ln \langle e^{-\beta(V_{\text{sol}})} \rangle_{\text{E,fix-id}} \quad. \tag{3.57}$$

This contribution can be evaluated in an NVT Monte Carlo simulation of the ideal Einstein crystal with fixed carrier particle.

3.2.3. Evaluation of ΔA_2

The third step in evaluating the free energy of the solid (equation (3.32)) is to compute the free energy difference ΔA_2 between the interacting Einstein crystal and the solid (both with fixed carrier particle). This term is evaluated using Hamiltonian thermodynamic integration as discussed in subsection 3.1. When going from

the Hamiltonian of the interacting Einstein crystal, $H_{\mathrm{E}}^{\mathrm{int}} = H_{\mathrm{E}}^{\mathrm{int}}(\boldsymbol{r}^N, \boldsymbol{r}'^N, \boldsymbol{p}^N, \psi^N)$, to that of the solid, $H_{\mathrm{sol}} = H_{\mathrm{sol}}(\boldsymbol{r}^N, \boldsymbol{p}^N)$, the harmonic springs have to be turned off gradually, which is achieved by tuning the coupling parameter λ from 1 to 0 in an analogous way as described in equation (3.14):

$$
\begin{aligned}
H(\lambda) &= \lambda H_{\mathrm{sol}} + (1 - \lambda)H_{\mathrm{E}}^{\mathrm{int}} \\
&= \lambda H_{\mathrm{sol}} + (1 - \lambda)(H_{\mathrm{E}}^{\mathrm{id}} + V_{\mathrm{sol}}) & (3.58) \\
&= K + \lambda V_{\mathrm{sol}} + (1 - \lambda)(V_{\mathrm{E}}^{\mathrm{id}} + V_{\mathrm{sol}}) \quad , & (3.59)
\end{aligned}
$$

where $K = K(\boldsymbol{p}^N)$, $V_{\mathrm{sol}} = V_{\mathrm{sol}}(\boldsymbol{r}^N)$ and $V_{\mathrm{E}}^{\mathrm{id}} = V_{\mathrm{E}}^{\mathrm{id}}(\boldsymbol{r}'^N, \psi^N)$. The change in the free energy is computed via equation (3.18):

$$
\Delta A_2 = \int_{\lambda=0}^{\lambda=1} \left\langle -V_{\mathrm{E}}^{\mathrm{id}} \right\rangle_{N,V,T} \, d\lambda \tag{3.60}
$$

Since the coupling constant Λ_{E} in the expression for the potential energy of the ideal Einstein crystal $V_{\mathrm{E}}^{\mathrm{id}}$ is a multiplicative factor (see equations (3.35)-(3.37)), it is convenient to include this parameter in the integration variable.

After performing a change in variable $\lambda \to \lambda \Lambda_{\mathrm{E}}$, the integral (3.60) takes on the following form, which gives us the **third contribution** to the free energy of the solid:

$$
\Delta A_2 = - \int_0^{\Lambda_{\mathrm{E}}} \frac{\langle V_{\mathrm{E}}^{\mathrm{id}} \rangle_{N,V,T}}{\Lambda_{\mathrm{E}}} \, d(\lambda \Lambda_{\mathrm{E}}) \tag{3.61}
$$

This integral can be evaluated with some numerical integration scheme; in this work we have used the Gauss-Legendre formula. NVT simulations have to be performed for different values of $\lambda \Lambda_{\mathrm{E}}$ ranging from 0 to the desired coupling strength, Λ_{E}, while keeping the carrier particle fixed to its lattice site.

3.3. Direct coexistence method

While free energy calculations involving the methods discussed above yield accurate results for coexistence points, the procedure requires many simulations and is thus quite involved, time-consuming and rather prone to errors.

As mentioned in the introduction to this chapter, the direct coexistence method [5] is a straightforward technique that requires simulations of the two phases in coexistence. Often, it is used to obtain melting points by putting fluid and solid phases into contact. A system in which half of the particles belong to the fluid, while the other half belong to the solid phase, is called an *interfacial system*, since its essential feature is the interface between those two phases. Simulations of the interfacial system can be performed in different ensembles and employing also different simulation techniques [5].

In the following, the description is restricted to the specific features of the simulations used in this work. As in all simulations in this work, we used the standard Metropolis Monte Carlo technique. For results of this technique for the IPC model, see section 4.4.3.

We now want to examine the three steps of the direct coexistence method by means of a particular system studied in this work:

Step 1. Solid equilibration:
The first step is to generate a solid of desired size (in our case, around 500 particles) and to let it relax to its equilibrium shape during a set of standard NpT simulations imposing different pressures and allowing the three edges of the simulation box to change independently, while keeping the angles between them fixed to guarantee an orthorhombic box.

Step 2. Interface creation / fluid equilibration:
In order to generate the fluid part of the interfacial system, we need to prepare a fluid structure with the same number of particles as in the solid structure. Furthermore, the simulation box has to have the same dimensions in x and y, so the two structures can later be put into contact.

It is convenient to use the solid structure obtained in **Step 1.**, which already has the right dimensions in x and y and melt that structure. This can be achieved

in NpT simulations at different pressures, allowing only the z-dimension of the simulation box to change.

However, when following this procedure, a small gap is introduced between the two phases when putting them together. Depending on the structure of the solid, this can lead to surface melting [13] and trigger melting of the solid below the actual melting point. If the solid is of a structure that facilitates this so-called premelting - open structures are especially prone to it - it is advisable not to equilibrate the two phases separately, but to proceed with a technique that generates a smooth boundary between the solid and the fluid.

In this technique, the phases are joined together *before* the fluid is equilibrated. Because of the periodic boundary conditions of the solid, the two parts of the system are separated by a smooth boundary. During equilibration of the liquid, this boundary is maintained by including the whole system in the simulation (*i.e.* the fluid and the solid part). Obviously, the solid part has to be left unchanged, since it is already equilibrated. This constraint can be incorporated into the algorithm in a simple way by excluding the solid particles from translational/rotational moves. When selecting a particle for a translational/rotational move, only those belonging to the fluid are considered.
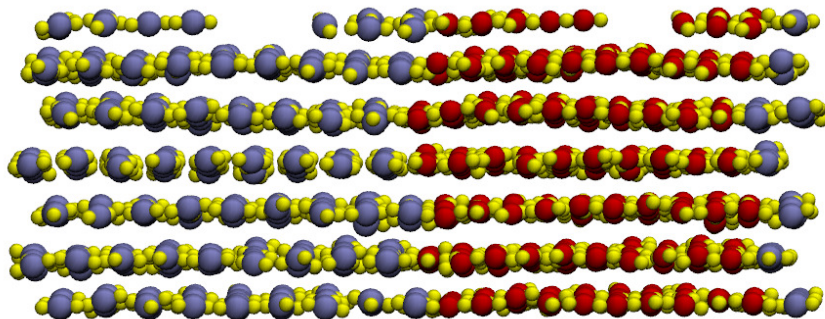
Figure 3.1.: Snapshot of a duplicated solid before liquid equilibration at $T^* = 0.159$ and $p^* = 0.286$

If we were to do NpT simulations, we would also have to apply a restriction to the volume moves, since the solid side of the system already has relaxed to its equilibrium volume - this would require some complex changes in the algorithm. However, if we know the equation of state $\rho_\text{fl}(p)$ for the fluid from a previous NpT

simulation, it is much faster and easier to scale the "liquid" part according to the respective volume, then join it together with the original solid before proceeding with NVT simulations. This scaling is done with respect to the z-direction, in order not to change the dimension of the interface between the two phases. Figure 3.1 shows a snapshot of a system that was prepared in this way. The solid phase at hand is a layered structure found in the IPC model with the parameters specified in table 2.1 in subsection 2.3. Half of the particles of the system shall belong to the liquid phase (grey color in figure 3.1), while the other half belongs to the solid phase (red color in figure 3.1). Of course, at this step of the process the "liquid" side of the structure is still in a solid-like structure, only expanded along the z-direction.

If the original solid has been simulated at a certain pressure p, with resulting box lengths x_{sol}, y_{sol} and z_{sol}, then the corresponding box length in z-direction for the fluid is

$$z_{\mathrm{fl}}(p) = \frac{N}{x_{\mathrm{sol}} \ y_{\mathrm{sol}} \ \rho_{\mathrm{fl}}(p)} \ , \tag{3.62}$$

where $\rho_{\mathrm{fl}}(p)$ is the density of the fluid that corresponds to the input pressure p. As can be observed by closely inspecting figure 3.1, for the pressure used in the simulation, $p^* = 0.286$, the boxlength in z-direction for the liquid is slightly larger than that of the solid, accounting for the lower density.

As soon as the interfacial system is set up, an NVT simulation of the liquid part (taking into account the restrictions on the translational/rotational moves mentioned above) can be started.
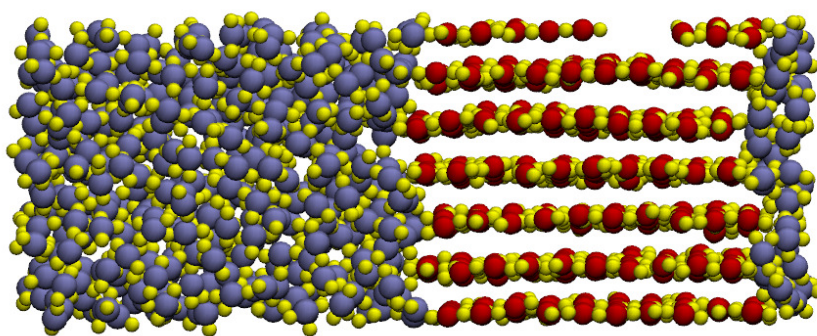
Figure 3.2.: Snapshot of the interfacial configuration shown in figure 3.1 after equilibration of the liquid at $T^* = 0.159$ and $p^* = 0.286$

This simulation can be performed at very high temperatures at first, so that the structure melts quickly. However, the actual equilibration of the liquid should be performed at the desired temperature. Figure 3.2 shows the system introduced in figure 3.1 after equilibration of the liquid side of the structure.

Step 3. Equilibration of the interfacial structure:
In the final step, the restriction on the translational/rotational moves is removed and all particles of the system are included in NpT simulations, imposing the same pressures used in the previous steps. If the input pressure differs from the (yet
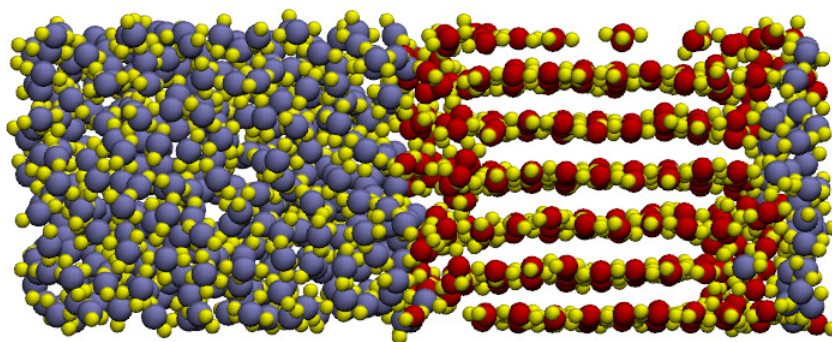
(a)
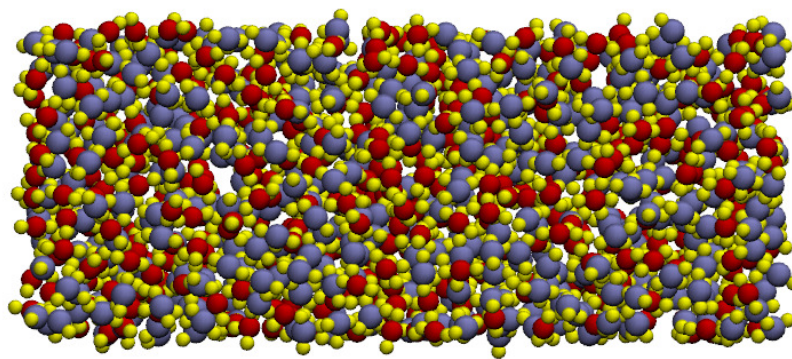
(b)

Figure 3.3.: Evolution of the interfacial configuration at $T^* = 0.159$ and $p^* = 0.286$ after (a) 3×10^3 (b) 5.1×10^5 steps

unknown) coexistence pressure, one of the two phases will grow in volume at the

cost of the other phase. Tracing the density evolution (or the visual representation of the resulting structures), one can observe which phase prevails for a given pressure.

By systematic variation of the imposed pressure, the coexistence pressure can be found in an iterative process. Figure 3.2 shows typical snapshots of the evolution of an intefacial system. For the temperature and pressure used in this simulation, the system evolved into a fluid.

As noted in the caption of figure 3.3, the system hadF completely evolved into a fluid after 5.1×10^5 steps. Since the coexistence pressure ($p^* = 1.595$) for those two phases lies considerably above the imposed pressure ($p^* = 0.286$), this evolution took place relatively fast. When getting closer to the coexistence pressure, it takes much longer for the system to fully evolve into one or the other phase.
Typical values for the number of required steps close to the coexistence point are in the order of $5 - 10 \times 10^6$ steps.

3.4. Gibbs-Duhem integration: Coexistence lines

Gibbs-Duhem integration is an efficient tool for evaluating coexistence lines and was first introduced in 1993 by Kofke [14].

It only requires knowledge of one coexistence point between the respective phases. Using a numerical integration scheme, the coexistence line can be traced starting from this initial point according to the *Clapeyron equation*, which we want to derive in the following.

We consider two phases (labeled 1 and 2) in coexistence at a specific temperature $T = T_1 = T_2$ and pressure $p = p_1 = p_2$. Hence, the following relation holds:

$$\mu_1(p, T) = \mu_2(p, T) \quad . \tag{3.63}$$

Changes in p, T and μ are correlated via the the Gibbs-Duhem relation [1]:

$$SdT - Vdp + Nd\mu = 0 \quad . \tag{3.64}$$

To guarantee that the two phases 1 and 2 to remain in coexistence, changes in temperature dT have to be compensated by changes in pressure dp. Since, along the coexistence line, the chemical potentials μ_1 and μ_2 are equal, their change as one proceeds from the coexistence point (p, T) to the coexistence point $(p+dp, T+dT)$ is equal as well:

$$d\mu_1(p, T) = d\mu_2(p, T) \quad . \tag{3.65}$$

Combining this equality with the Gibbs-Duhem relation (3.64), we obtain:

$$-\frac{S_1}{N_1} dT + \frac{V_1}{N_1} dp = -\frac{S_2}{N_2} dT + \frac{V_2}{N_2} dp \tag{3.66}$$

With the definitions of the specific entropy $s = S/N$ and the specific volume $v = V/N$ we can rearrange this expression to yield the *Clapeyron equation*:

$$\frac{dp}{dT} = \frac{s_1 - s_2}{v_1 - v_2} \quad . \tag{3.67}$$

With the Maxwell relation $T = \left(\frac{dH}{dS}\right)_P$, this expression can be rewritten as:

$$\frac{dp}{dT} = \frac{h_1 - h_2}{T(v_1 - v_2)} \quad , \tag{3.68}$$

---

[1] the derivation of the Gibbs-Duhem relation can be found in Appendix A.3

where $h = H/N$ is the specific enthalpy. Equation (3.68) is a first-order differential equation that describes the change in pressure upon a change in temperature in order to maintain coexistence between the two respective phases. Since we do not have an analytical expression for the dependence of the specific enthalpies h_1 and h_2 and the specific volumes v_1 and v_2 on p and T, we can only evaluate the right side of the differential equation (3.68) at discrete coexistence points (p, T) by performing NpT simulations. To this end, a numerical scheme has to be applied in order to evaluate the coexistence line.

Several numerical schemes can be applied in order to tackle Gibbs-Duhem integration (and differential equations in general), among which predictor-corrector methods are particularly suitable. In this work, we made use of a fourth-order Runge-Kutta algorithm with either T or p acting as the independent variable, depending on the slope of the coexistence line [2]. Since every evaluation of the right side of equation (3.68) requires two NpT simulations and is therefore very time-consuming, the Runge-Kutta scheme is very well suited, since it requires relatively few of these evaluations (compared to other numerical integration schemes). For more insight on Runge-Kutta methods and on the numerics of ordinary differential equations in general, see reference [?].

---

[2]While in the above derivation, it is implied that T is the independent variable, in cases where the coexistence line exhibits a large slope in the p/T plane (*i.e.* small changes in temperature yield large changes in pressure), it is more convenient to let the pressure act as the independent variable and to integrate the Clapeyron equation in the following way: $\frac{dT}{dp} = \frac{T\Delta v}{\Delta h}$.

3.5. Simulation Algorithm

In all simulations performed for this thesis, we used the standard Metropolis Monte Carlo technique [15]. Our code allows for either NpT or NVT simulations (see line from input file below). For all simulations, we used systems of roughly 500 particles in orthorhombic simulation boxes. Except for simulations within the *Einstein molecule method* (see section 3.2), all simulations were performed using periodic boundary conditions and minimum image convention.

In this text, the term *Monte Carlo step* refers to N attempts to displace *or* rotate one random particle (N being the total number of particles) plus, in the case of NpT simulations, one attempt to change the volume. Obviously, depending on the problem, the number of necessary steps differs and is explicitly stated in section 4 for each simulation mentioned.

Our code allows for different types of volume changes, characterized by the way in which the lengths of the three edges of the box, l_x, l_y and l_z, change. Apart from the fact that in some of those types of volume moves, one or two of the edges are kept unchanged, there is also the possibility of assigning different values of $\Delta l_{\max}$ to the three edges. $\Delta l_{\max}$ is the amount by which one edge can maximally change during one volume move. Depending on the structures involved in the simulation, we used one of the following types of volume moves:

- l_x, l_y and l_z change independently, but assuming the same value for $\Delta l_{\max}$, keeping the orthorhombic setup (used for interfacial systems, see section 3.3)

- l_x, l_y and l_z change by the same amount, assuming the same value for $\Delta l_{\max}$ (*cubic symmetry* - used for fluids and fcc-structures)

- only l_z changes, l_x and l_y remain fixed (used for equilibration of the fluid in the direct coexistence method, see section 3.3)

- l_x and l_y change assuming the same value for $\Delta l_{\max}$, l_z changes with a separate $\Delta l_{z,\max}$ (used for the layered solid)

l_x, l_y, l_z and $\Delta l_{\max}$, as all lengths used in our simulations, are always expressed in units of the boxlength in the respective direction. Note that the value of $\Delta l_{\max}$ for each direction is not constant throughout the simulation (neither is the maximum rotation or the maximum displacement). The code has a mechanism that regularly

adjusts the maximum displacement, the maximum rotation and the maximum change in boxlength in a way that guarantees acceptance ratios of around 40%. However, the starting values for $\Delta l_{\max}$ for each direction are passed on to the program via an input-file. The respective line in the file reads:

dmax	omax	vmax1	vmax2	vmax3	temp	pres	npt	iscale	iseed
0.04	0.1	0.005	0.005	0.005	1	1	.true.	2	-28376

Where **dmax** is the maximum displacement of a particle, **omax** is a measure for the maximum change in orientation and **vmax1**, **vmax2** and **vmax3** are the maximum changes in boxlength for each direction (labeled $\Delta l_{\max}$ above). These values will be adjusted throughout the simulation (see above). **temp** and **pres** are the input columns for temperature and pressure, while **iscale** specifies the type of volume changes - in this case, "2" corresponds to cubic scaling (see above). **npt** specifies whether the simulation is performed in the NVT or in the NpT ensemble, **iseed** is an input for the random number generator in the algorithm.

4. Results

4.1. Candidate structures

For the set of model parameters used in the work for this thesis (see table 2.1), two solid structures were identified at vanishing temperature with the help of an optimisation technique based on evolutionarly algorithms [11]. Those structures served as a starting point for our calculations at finite temperatures.

- Layered solid:
  The layered solid, see figure 4.1, is a structure composed of 2D layers that are separated by a distance that is significantly larger than the equilibrium distance between the particles within the layers.

(a)   (b)
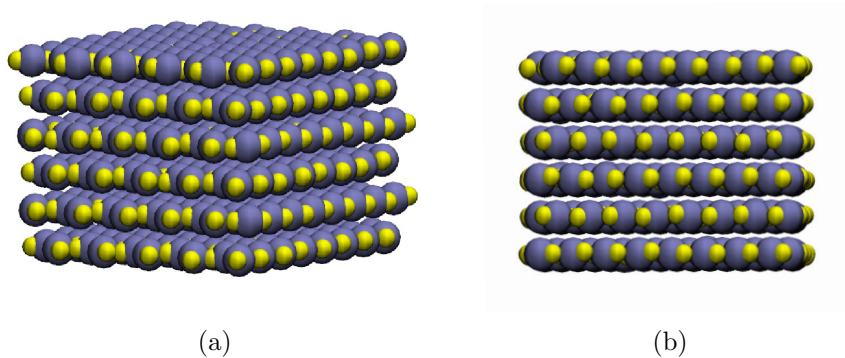
Figure 4.1.: Typical snapshots of a layered solid structure of 500 particles;
(a) perspective snapshot (b) view in y-direction

- fcc structure

  Figure 4.2 shows a typical snapshot for an fcc structure with 500 particles.

<div align="center">(a)   (b)</div>
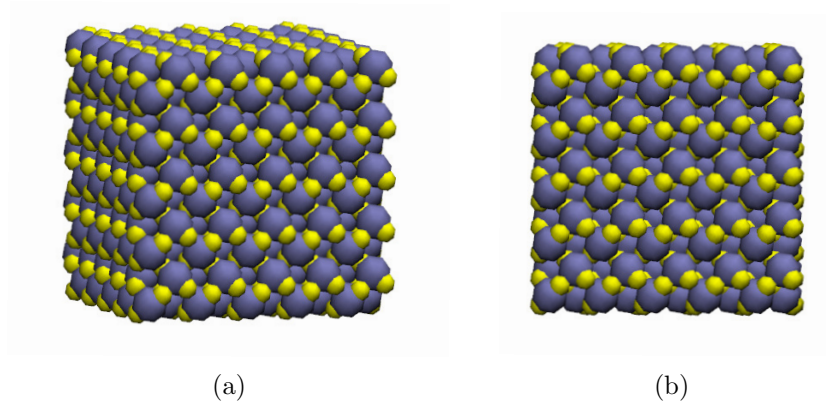
Figure 4.2.: Typical snapshots of the fcc structure with 500 particles;
(a) perspective snapshot (b) view in y-direction

- fcc plastic crystal - "fccp"

  When examining the fcc solid at finite temperatures, it soon became obvious that the IPC system forms an additional solid with an fcc-structure. This solid is a *plastic fcc crystal*, which means that the spatial order of the particles is the same as in the fcc structure, but they lack orientational order, comparable to the fluid phase.

<div align="center">(a)   (b)</div>
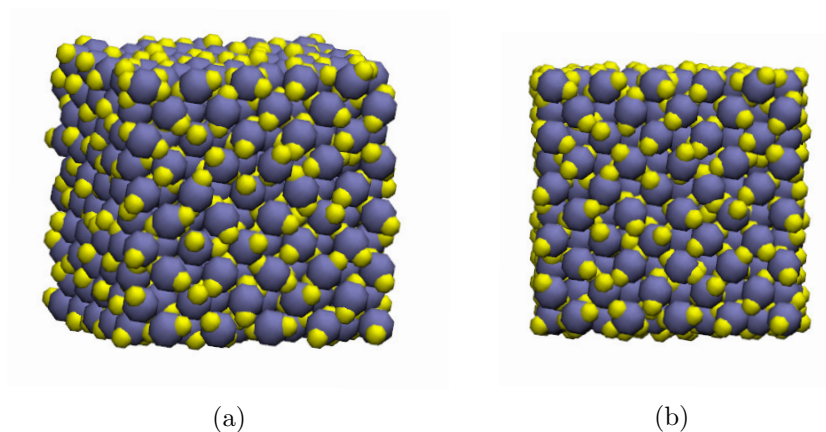
Figure 4.3.: Typical snapshots of the fcc plastic crystal structure of 500 particles;
(a) perspective snapshot (b) view in y-direction

Comparing figure 4.3, which shows such a strucuture, to the fcc crystal in figure 4.2 helps clarify the difference between those two fcc phases. In the following, the fcc plastic crystal is referred to as "fccp".

- fluid phase

  The fourth phase formed by IPCs with the parameters of table 2.1 is the fluid phase. The fluid is characterized by both spatial and orientational disorder, as can be seen in figure 4.4, which shows a typical snapshot of a fluid configuration. At low temperatures ($T^* \leq 0.159$) we found indications of a vapour-liquid transition, which we did not investigate further, since the calculation of the exact location of this transition requires special techniques that go beyond the scope of this thesis.
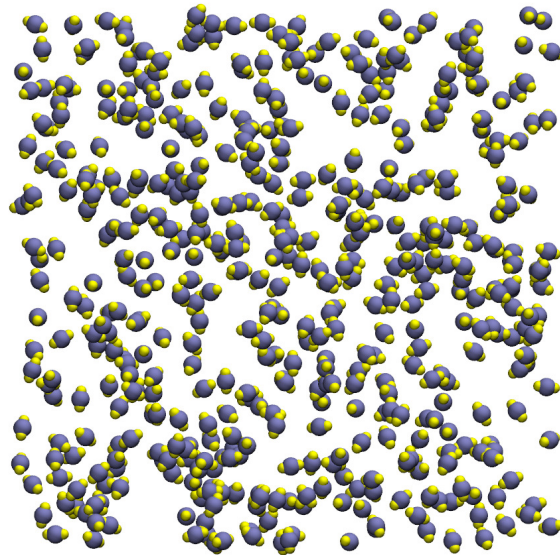
Figure 4.4.: Typical snapshot of an IPC fluid

4.2. Exploratory simulations - Regions of stability

In this section, we present results from exploratory simulations, yielding estimates for the regions of stability of the respective phases. We performed NpT simulations and examined the behaviour of the phases upon increasing pressure values at constant temperature (see subsection 4.2.1) and upon heating and cooling the system at constant pressure (see 4.2.2).

However, for most structures, simulations of this kind can only provide rough estimates for transition points, since hysteresis effects have to be taken into account. The transition from one stable phase into another will not always occur exactly on the phase boundary determined by the condition of equal chemical potentials of the respective phases. Instead, hysteresis is encountered in simulations (and also in experiments), which means that a phase may remain intact well beyond the actual transition point. Obviously, this is only true for intermediate simulation lengths. Eventually, the system will transform into the phase with lowest chemical potential. The region where a phase has the lowest chemical potential of all phases exhibited by the system is its region of *thermodynamic stability* and can only be evaluated by free energy calculations. The stability of a phase beyond its range of thermodynamic stability, is often referred to as *mechanical stability*.

4.2.1. Regions of stability - isotherms

In order to obtain a rough estimate of the temperature and pressure ranges in which a particular phase is stable, we performed NpT simulations along isotherms, scanning different ranges of pressure and evaluating the equation of state $\rho(p)$. Apart from providing estimates for the ranges of stability, those simulations at fixed temperature are also essential for thermodynamic integration along isotherms (see section 3.1.3).

In the equation of state $\rho(p)$, discontinuous changes in the density are an indication for a first-order phase transition at the respective pressure.
The term *first-order phase transition* goes back to *Paul Ehrenfest (1880-1933)*. He classified phase transitions according to the behaviour of the partial derivatives of

the thermodynamic potentials at the transition points. If the *first* derivative of the thermodynamic potential is discontinuous at the transition point, the respective phase transition is called a *first-order* transition. This classification, although slightly outdated, is still widely in use and is applicable to our case:

The ensemble average of the volume $\langle V \rangle$ in the isothermal-isobaric ensemble is the *first* derivative of the Gibbs free energy $G(N, p, T)$ with respect to the pressure p (at constant T and N):

$$\langle V \rangle = \left(\frac{\partial G}{\partial p} \right)_{T,N} \quad . \tag{4.1}$$

Since we define the total number density in our system as $\rho = {}^N\!/\!{}_{\langle V \rangle}$, phase transitions associated with a jump in density are of *first order*.
The pressures at which those discontinuities in the density occur serve as estimates for the coexistence pressures and thus help defining the regions of stability of the respective phases.

Despite the hysteresis effects mentioned above, NpT simulations at different temperatures and pressures are ideal starting points for exploring the phase behaviour of the system at hand.

We performed isothermal simulations at several temperatures. Results for two of them are shown in the following - $T^* = 0.095$ and $T^* = 0.159$. The number of Monte Carlo steps used in those simulations was in the oder of $5 - 10 \times 10^6$.

Isotherms at $T^* = 0.095$:
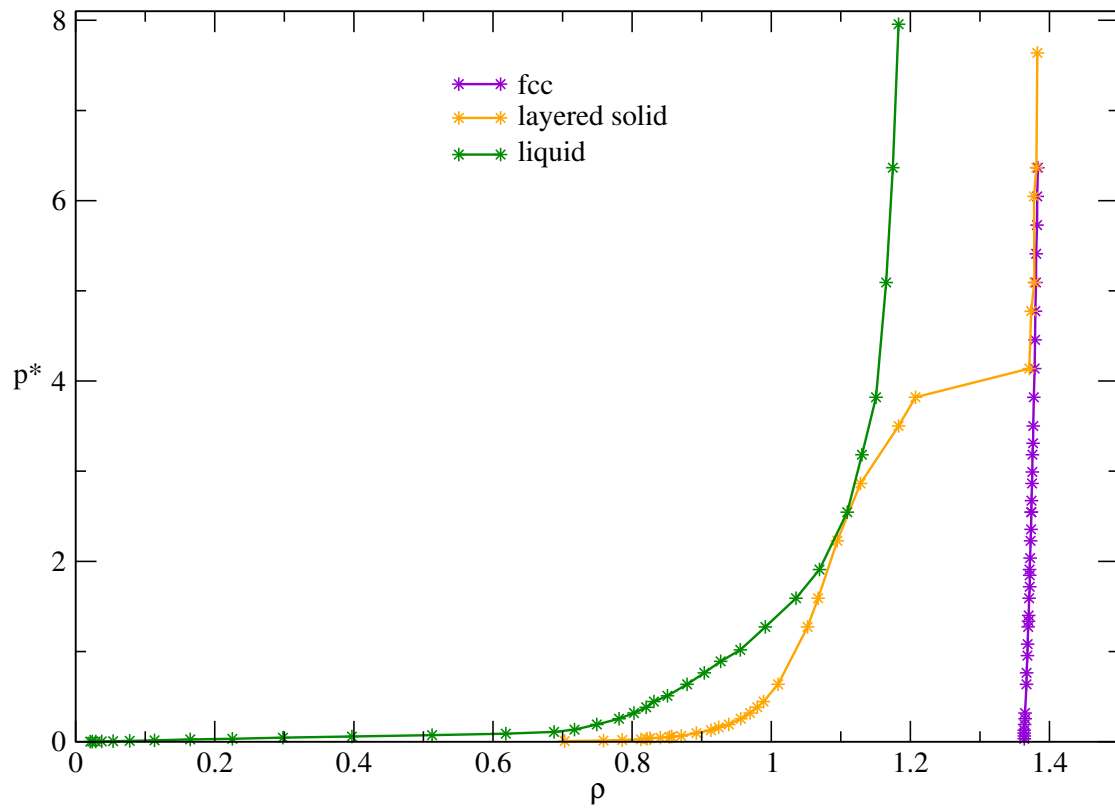
Figure 4.5.: Pressure for an IPC system along the isotherm at $T^* = 0.095$ as a function the density for the three different phases (as labeled)

In figure 4.5, we show the equation of state $p^*(\rho)$ along the isotherm $T^* = 0.095$. With the data obtained from our simulations, at this temperature, we did not observe melting for either the layered solid or the fcc structure. However, there is a transition from the layered solid to the fcc, which is located at pressure values around $p^* \approx 4.10$.

Isotherms at $T^* = 0.159$:
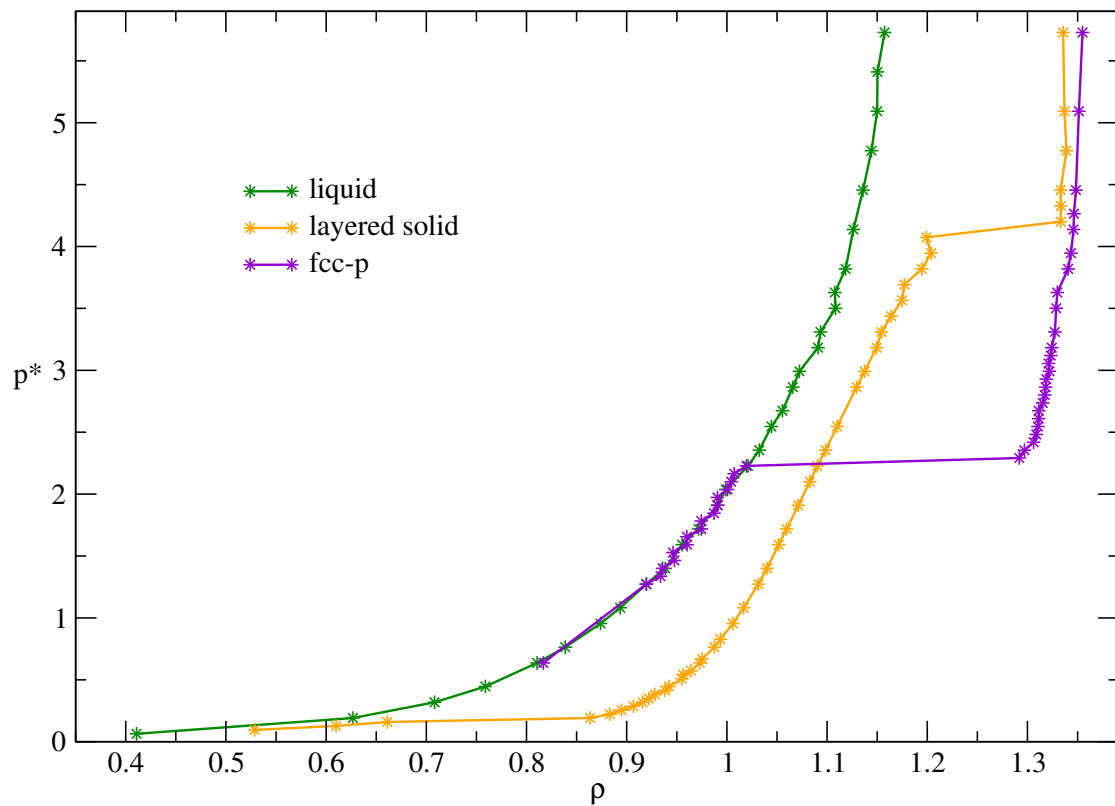
Figure 4.6.: Pressure for an IPC system along the isotherm at $T^* = 0.159$ as a function of the density for the three different phases (as labeled)

In figure 4.6, we show the pressure along the isotherm at $T^* = 0.159$. According to our results, at this temperature, the fccp structure melts at pressure values around $p^* \approx 2.25$. At a higher pressures (between $3.5 < p^* < 4$), a small discontinuity in the density accounts for the transition to the ordered fcc structure. The layered solid exhibits a melting point in the low-pressure region at $p^* < 0.09$. It is not possible to evaluate the melting point more accurately from the data shown in figure 4.6. Furthermore, the layered solid undergoes a transition towards the ordered fcc structure at pressures around $p^* \approx 4.15$.

4.2.2. Estimates of melting temperatures - isobars

In addition to NpT simulations along isotherms, simulations along isobars also yield valuable information about the regions of mechanical stability. In this subsection, we show two sets of data obtained by exploratory simulations in order to estimate the melting temperature at different pressures for the layered solid as well as for the fcc structure.

Melting of the layered solid:

Figure 4.7 shows the results for the density ρ for NpT simulations during which the layered solid was heated up at three different values of pressure.
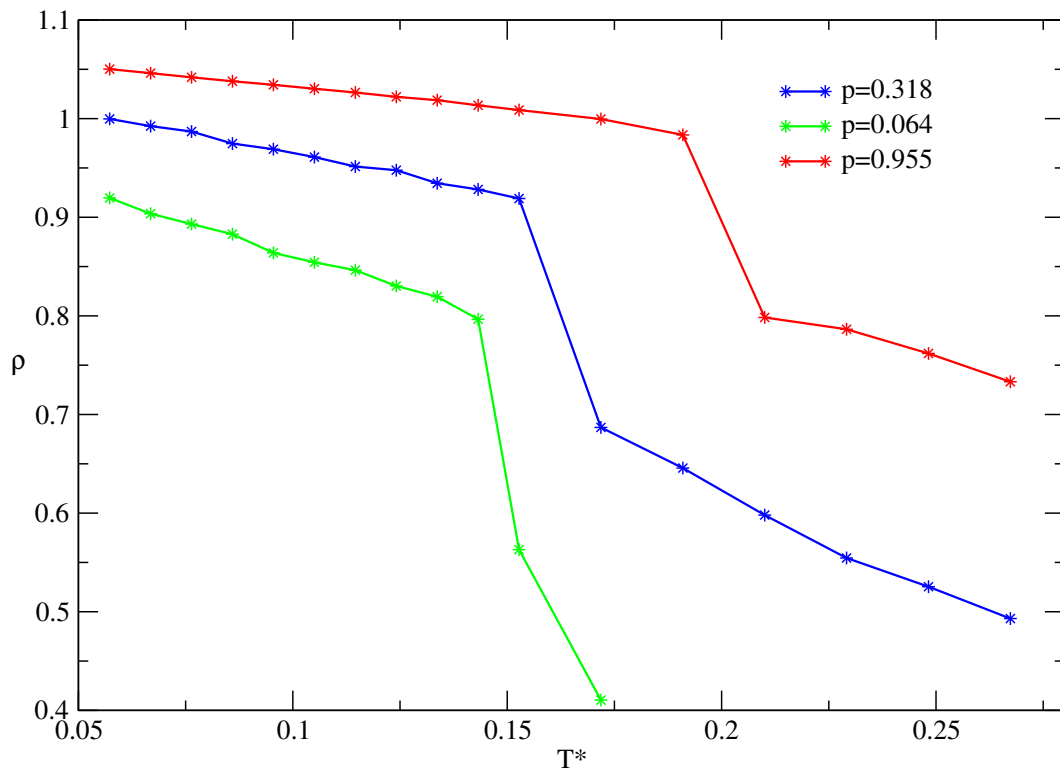
Figure 4.7.: Density as a function of temperature obtained in NpT simulations for three different pressures (as labeled)

The data obtained from these simulations allow for first estimates of the melting temperature of the layered solid, which is characterized by a discontinuous change

in density. We can estimate the occurrence of this transition at $T^* \approx 0.14$ for $p^* = 0.064$, at $T^* \approx 0.16$ for $p^* = 0.318$ and at $T^* \approx 0.20$ for $p^* = 0.955$. The data shown was obtained with roughly 10^6 Monte Carlo steps.

Melting of the fcc structure:

Figure 4.8 shows the results for the density ρ for NpT simulations during which the fcc structure was heated up at three different values of pressure. The fcc crystal does not melt directly, but via a transition to either the plastic crystal [1] or - at lower pressures - the layered solid.
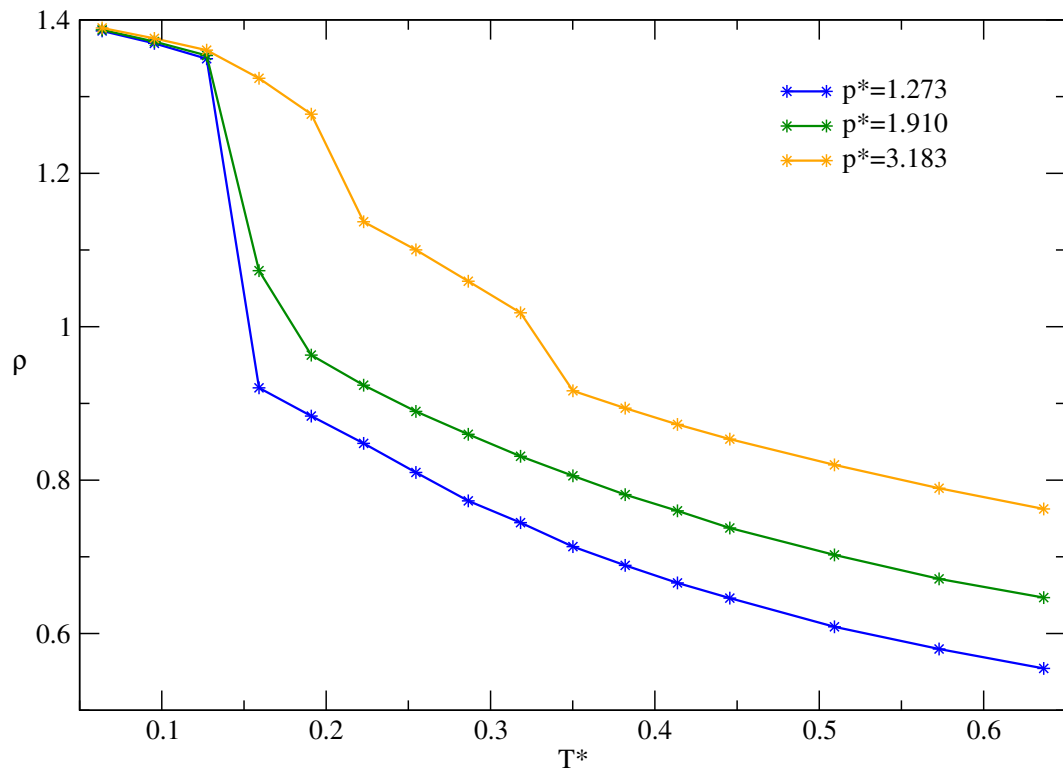
Figure 4.8.: Density vs. temperature for three different pressure values; the kinks provide estimates of the melting temperature for the fcc structure

---

[1] For results of isobaric simulations exploring the change between the fcc and the fccp structure in detail, see subsection 4.4.2.

In figure 4.8, the result for the density function at the highest pressure value, $p^* = 3.183$, exhibits a behaviour that corresponds to a "reconstruction" to the fccp solid, before the structure finally melts. This reconstruction takes place between temperatures $T^* \approx 0.15$ (which serves as an estimate for the transition temperature between the fcc and the fccp structure) and $T^* = 0.318$ (which is an estimate for the melting temperature of the fccp structure).

The results for the two lower pressure values depicted in 4.8 are a special case. The data obtained from those simulations imply a direct melting of the fcc without reconstruction to another solid, the corresponding melting temperatures being approximately $T^* \approx 0.14$ at pressure $p^* = 1.273$ and $T^* \approx 0.16$ at pressure $p^* = 1.910$. However, from the phase diagram (see section 4.5) we know that the fcc is not thermodynamically stable for the initial pressure and temperature values used in this simulation, since those values correspond to the region of thermodynamic stability for the layered solid. Due to its mechanical stability in this region, the solid stays in fcc structure until finally breaking down and melting at the respective temperatures.

This issue is a good example for the fact that, due to hysteresis effects, simple NpT simulations are not a suitable method for complete evaluation of phase diagrams. Particularly, knowledge of candidate structures is crucial, in order to avoid overlooking certain phases.

The data shown in figure 4.8 was obtained with simulations of roughly 10^6 Monte Carlo steps.

Angular distribution function

We can use the change in orientational order that the fcc undergoes when melting to analyze the phase transition in more detail. This is especially important when looking at the fcc-fccp transition (see subsection 4.4.2), but can also be useful in order to determine if the fcc structure has indeed melted.

In order to quantify the orientational order, we have evaluated the *angular distribution function*, which gives the probability that the axis of particle encloses a certain angle θ with a reference orientation.
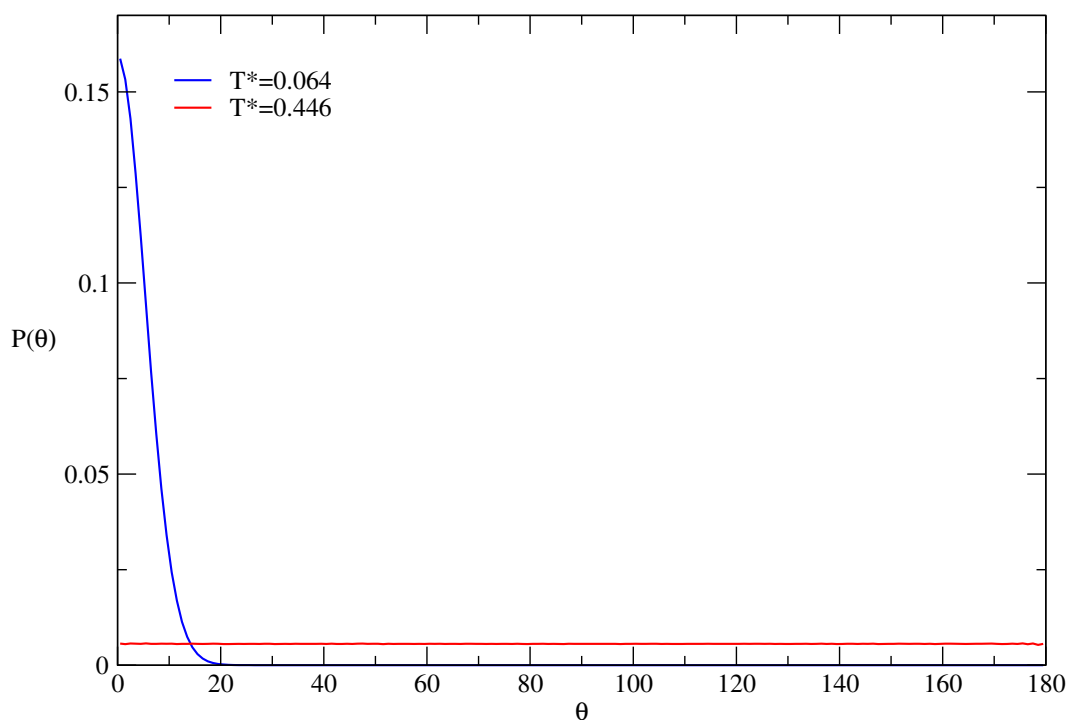
Figure 4.9.: Angular distribution functions $P(\theta)$ of the fcc and the liquid phase; depicted is the probability of a particle enclosing a certain angle with the orientation of its respective particle in the ordered fcc structure.

In figure 4.9, this probability is denoted by $P(\theta)$. As a reference, we have used the equilibrium fcc crystal structure at the lowest temperature considered in our simulations. While heating up the fcc structure, we have calculated the probability that the orientation of a particle encloses a certain angle θ with its equivalent

particle in the equilibrium fcc crystal.

In figure 4.9 we show the angular distribution function for the highest pressure considered ($p^* = 3.183$) at two temperatures - one considerably lower than the presumable coexistence temperature, the other considerably higher.

We can see that for those two cases, the angular distribution functions are completely different: for the fcc structure it shows a pronounced peak around $\theta = 0\,^\circ$, while after melting, i.e. in the liquid phase, which lacks orientational order, it is a uniform distribution. For the corresponding angular distribution functions in the fcc-fccp transition see figure 4.15 in subsection 4.4.2.

4.3. Free Energy Calculations

In the following section, the process of obtaining the value of the free energy at a certain state point (T, ρ) is described. As discussed in section 3, the free energy is needed only for one state point in order to obtain the dependence of the free energy on the pressure by thermodynamic integration. Section 4.4 explains how to obtain coexistence points from those results or with the alternative direct coexistence method explained in 3.3. Note that we calculate free energies in units of $N k_\mathrm{B} T$ and the chemical potential in units of $k_\mathrm{B} T$. We define

$$A^* = \frac{A}{N k_\mathrm{B} T}$$
$$\mu^* = \frac{\mu}{k_\mathrm{B} T} \quad,$$

which are both dimensionless expressions.

Error in free energy calculations

Since free energy calculations require complex techniques, the results have to be analyzed with respect to their accuracy. To this end, two issues have to be considered:

- *Statistical error*
  The accuracy of the results depends on a number of factors, among which simulation lengths and the number of points along the integration paths play a key role. Calculating the error using the appropriate methods is a very cumbersome procedure in the context of free energy calculations, since many calculations are involved and the propagation of errors has to be traced. The calculation of the actual error is thus beyond the scope of this thesis, however it would be important to calculate it eventually.

- *Systematic error*
  Since free energy calculations involve several steps, mistakes can easily occur without being immediately noticed. Therefore, it is important to have some

methods at hand that can be applied in order to test the results.

In this work, we applied two types of checks:

(i) An obvious check is calculating the free energy with two different methods and comparing the resulting values. We applied this check whenever we had two different methods at hand for the respective calculation.

(ii) We also tested our results for *thermodynamic consistency*: If free energy calculations were performed at two different state points (*e.g.* the same temperature, but different densities ρ_1 and ρ_2), the equation of state at the respective temperature can be used to perform thermodynamic integration along this isotherm (see section 3.1.3) from ρ_1 to ρ_2. The result for the free energy from this integration can then be compared to the the one obtained from the original calculations performed at ρ_2.

Both of these checks yield two results for the free energy that are slightly different due to statistical uncertainty in the simulations. However, if their difference exceeds a value that can be explained in the scope of statistical uncertainty, systematic error has occurred in the calculation of one of the values, or even both.

For the calculations discussed below, details about the employed consistency checks are given and the values for the respective deviations in free energy $\Delta A^*/A^*$ are specified. All of those deviations are sufficiently small to confidently assume that they can be explained in the scope of statistical uncertainty[2]. Thus, we can rule out systematic error in the following results.

---

[2] However - as already stated above - proper error calculation has to be performed in order to confirm this assumption.

4.3.1. Fluid phase

For free energy calculations in the fluid phase, we applied three different methods:

I. **thermodynamic integration from the ideal gas along $T^* = 0.318$**

   This procedure was carried out as described in section 3.1.3, integrating from the ideal gas ($\rho = 0$) along the isotherm at $T^* = 0.318$. Along this isotherm, we do not encounter any phase transitions. Particularly, the vapour-liquid transition mentioned in section 4.1 is located at lower temperatures, so thermodynamic integration is possible along this direct path. We performed NpT simulations, using a total of 10^6 MC steps. The result of these simulations will be shown in figure 4.12 of section 4.4 in the context of evaluating the coexistence point with the fccp structure.

II. **thermodynamic integration along a combined path:**
   isotherm $T^* = 0.318$ + isochore $\rho = 0.798$ + isotherm $T^* = 0.159$

   Our first objective was to evaluate the free energy at temperature $T^* = 0.159$. However, integration from the ideal gas ($\rho = 0$) to the desired density was not possible due to the vapour-liquid transition at this temperature. Consequently, we had to design an integration path that avoids this transition. While method I. is only valid for supercritical temperatures, it is always possible to construct a combined path of isotherms and isochores in order to avoid phase transitions. Thermodynamic integration was performed along the supercritical isotherm at $T^* = 0.318$ until the desired density ($\rho = 0.798$) was reached. From NVT simulations at this density, we could integrate along the isochore $\rho = 0.798$ down to the temperature $T^* = 0.159$. For the simulations along the path, we used a total of 10^6 MC steps. The integration path is shown in figure 4.10.

III. **thermodynamic integration along paths of $\beta^* p^* = const.$ [3]**

   As described in subsection 3.1.3, integration along paths of $\beta^* p^* = const.$ can be used to link the chemical potential of the IPC fluid to that of the

---

[3] $\beta^* p^*$ is expressed in units of $(2\sigma)^3$, see Appendix A.1

hard sphere fluid at high temperatures. The reference values for the chemical potential of the hard sphere fluid were taken from reference [16]. The hard sphere system is in the fluid phase for pressures below $\beta^* p^* = 11.54$ [5], so we chose $\beta^* p^* = 4$ and $\beta^* p^* = 10$ as integration paths. For these simulations we used a total of 4×10^6 MC steps.

Note that this method also avoids the vapour-liquid transition discussed above. The method is valid at all temperatures, as long as no phase transition is crossed (this can be ensured by an appropriate choice of β^* and p^*). In order to evaluate the free energy at $T^* = 0.159$, in addition to method II., we also integrated along $\beta^* p^* = 4$ to the state point of interest ($T^* = 0.159, \rho = 0.798$), which served as a valuable consistency check, see below. The two paths I. and II. leading to the same state point are shown in figure 4.10.

Consistency checks

Since we studied the free energy of the fluid extensively, we had several means that enabled us to verify the results obtained from the methods above. In the following, we present some consistency checks we performed in order to reduce the risk of mistakes remaining unnoticed. We conducted three comparisons among the three methods explained above:

- Comparison between methods I. (isotherm $T^* = 0.318$) and III. ($\beta^* p^* = 4$):

  As specified in the following table, we obtained excellent agreement between methods I. and III. at the state point ($T^* = 0.318, \rho = 0.743$). The density to which we integrated from the ideal gas in method I. was predetermined by the result of the simulations at $\beta^* p^* = 4$. The results are specified in the below table, including the deviation in free energy:

method	T^*	p^*	ρ	A^*	$\Delta A^*/A^*$
I.	0.318	1.277	0.743	0.93095	0.0019
III. ($\beta^* p^* = 4$)	0.318	1.273	0.743	0.92916	

- Comparison between $\beta^* p^* = 4$ and $\beta^* p^* = 10$ (method III.):

  We also tested the results obtained from the two routes realized for method III. ($\beta^* p^* = 4$ and $\beta^* p^* = 10$) for thermodynamic consistency. The comparison was conducted at $T^* = 0.127$. In order to cross-check the results obtained from those two routes, we first evaluated the free energy via one route at $T^* = 0.127$ (and at the density corresponding to that temperature in the respective route). Then, we performed thermodynamic integration to the density that corresponds to that temperature in the other route. This thermodynamic consistency check was performed for both routes:

method	T^*	ρ	A^*	A^* from TDI	$\Delta A^*/A^*$
III. ($\beta^* p^* = 4$)	0.127	0.8256	-3.06796	-3.09025	0.0072
III. ($\beta^* p^* = 10$)	0.127	0.9548	-1.99248	-1.97019	0.0112

- Comparison between routes II. and III. ($\beta^* p^* = 4$):

  The third check we performed was between the constructed route II. described above and the path along $\beta^* p^* = 4$ (method III.). As mentioned above, we evaluated the free energy at the state point ($T^* = 0.159, \rho = 0.798$). Figure 4.10 depicts the two integration paths in the T^*/ρ plane. The results from both routes are summarized in the following table, including the deviation in free energy:

method	T^*	p^*	ρ	A^*	$\Delta A^*/A^*$
II.	0.159	0.642	0.814	-1.19251	0.0260
III. ($\beta^* p^* = 4$)	0.159	0.637	0.814	-1.16195	
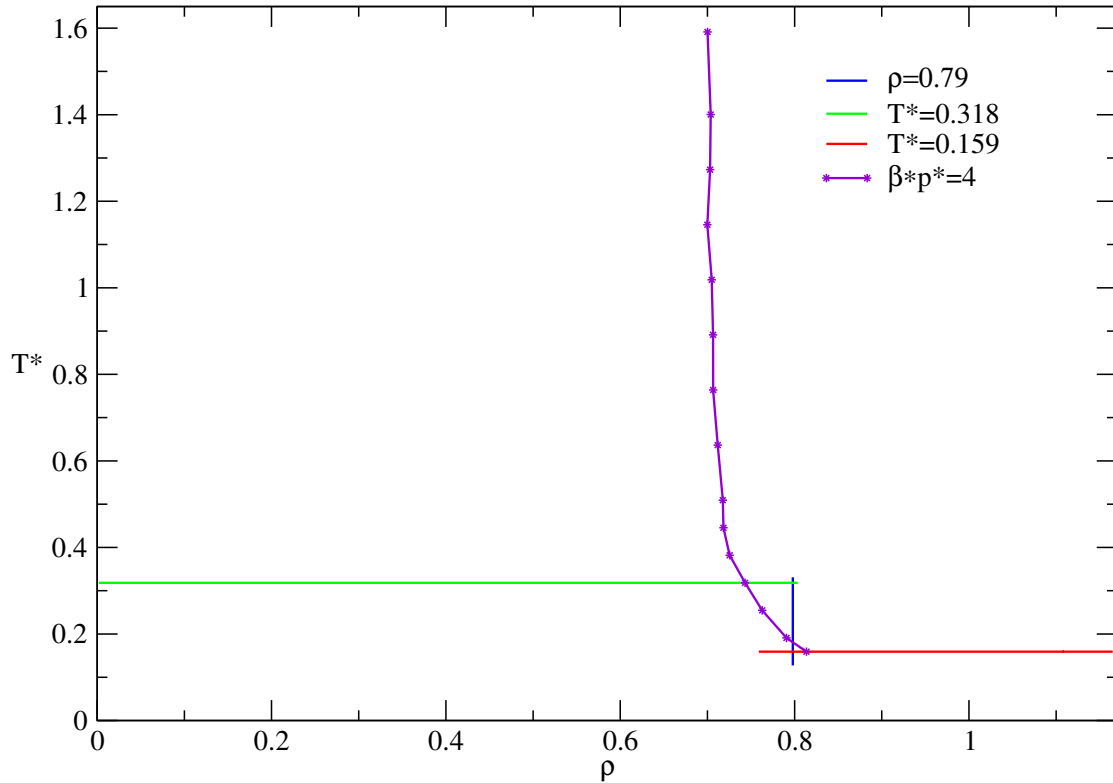
Figure 4.10.: Two alternative integration paths in the (T^*, ρ) plane (methods II. and III.) leading to the state point $(T^* = 0.159, \rho = 0.798)$; those paths were used for evaluating the free energy of the fluid via thermodynamic integration while avoiding the liquid-vapour transition in the low-density regime at $T^* = 0.159$.

4.3.2. FCC plastic crystal

For the fccp structure, the $\beta^* p^* = const.$ method described in subsection 3.1.3 was used to obtain the chemical potential and, consequently, the free energy. Calculations were conducted both for $\beta^* p^* = 16$ and $\beta^* p^* = 20$ using the hard sphere fcc system as a reference system at high temperatures. For the coexistence pressure for hard spheres we assumed the value $p^* = 11.54$ [5], which is well below the values we have chosen for our simulations, so the hard sphere fcc crystal is a suitable reference system. The reference values for the chemical potential of the

hard sphere solid were taken from [17].

Figure 4.11a shows the two paths in the p^*/β^* plane, while figure 4.11b depicts the dependence of the internal energy per particle, u^*, on β^*. Simulations were performed from high temperatures ($T^* = 5.787$) down to temperatures of $T^* = 0.318$. With equation (3.24) from section 3.1.3, the chemical potential at any temperature (and at the corresponding density) along the path can be evaluated.

In order to verify that the IPC system was indeed behaving as a hard sphere solid at high temperatures, we compared the density of our system at the highest temperature simulated ($T^* = 5.787$ with $p^* = 92.588$, so $\beta^* p^* = 16$) with that of the hard sphere fcc system at $\beta^* p^* = 16$:

$$\rho_{\mathrm{HS}} = 1.122$$
$$\rho_{\mathrm{fccp}} = 1.124 \; ,$$

which is a satisfactory agreement. For $\beta^* p^* = 20$ we obtained an agreement of similar quality.

For the NpT simulations at $\beta^* p^* = const.$ we used a total of 10^6 MC steps. The dependence of the chemical potential of the plastic fcc crystal on the pressure will be shown in figure 4.12 (in section 4.4).

Consistency checks

- Thermodynamic consistency test: comparing $\beta^* p^* = 16$ and $\beta^* p^* = 20$
  We tested our results from both routes described above for thermodynamic consistency. In the following table we explicitly show the results from our calculations, including the deviation in free energy:

method	T^*	ρ	A^*	A^* from TDI	$\Delta A^*/A^*$
$\beta^* p^* = 16$	0.318	1.1757	5.5444	5.5752	0.0055
$\beta^* p^* = 20$	0.318	1.2401	6.3725	6.3416	0.0049
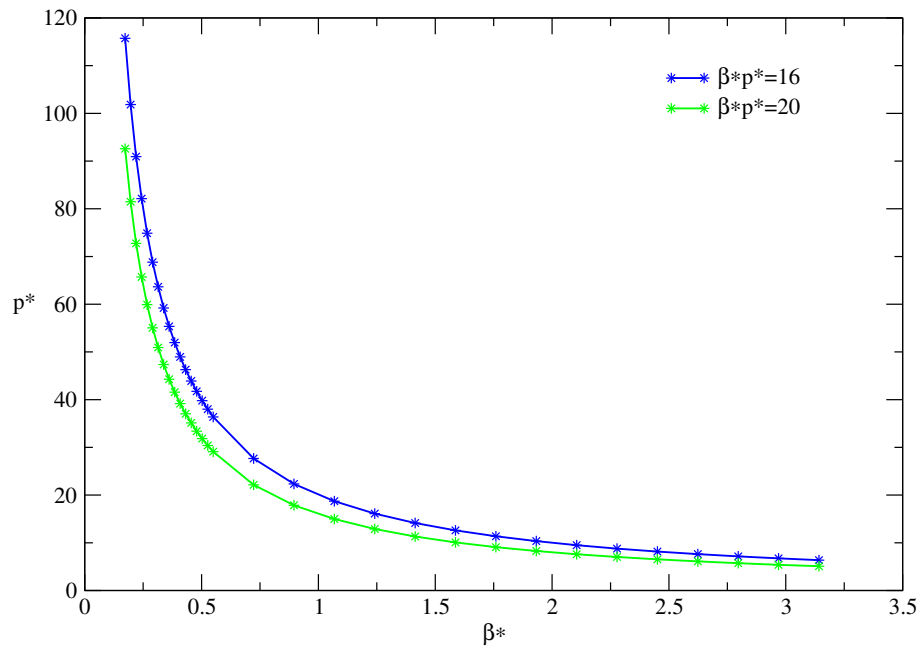
(a)
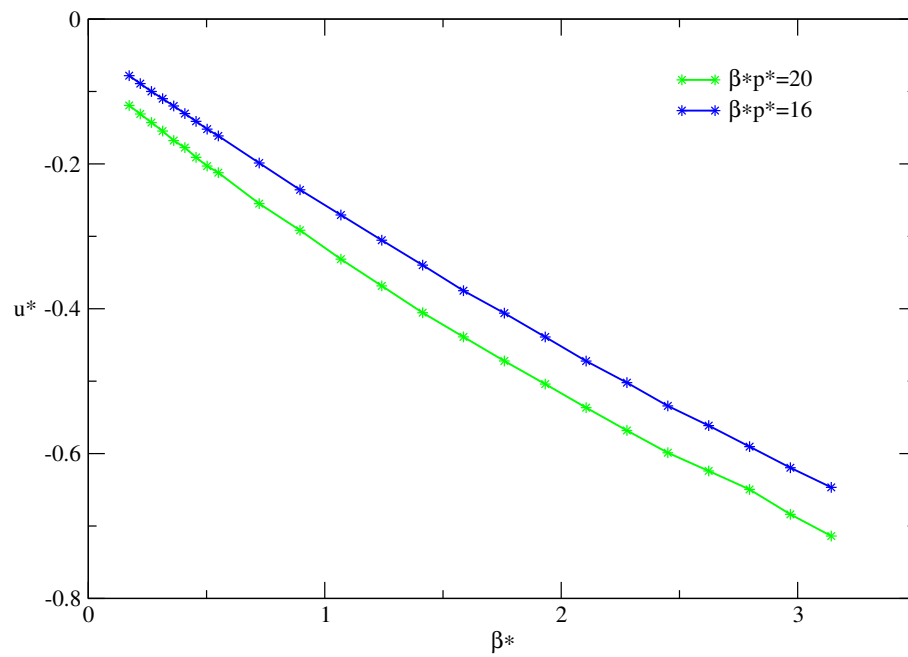
(b)

Figure 4.11.: (a) Depiction of the state points visited by the two integration paths used for evaluating the free energy of the fccp at $T^* = 0.318$ ($\beta^* = 3.145$); $\beta^* p^* = const.$ (specified in the legend)

(b) Depiction of the integrand $u(\beta^*)$(see equation (3.24)) used to evaluate the free energy of the fccp at $T^* = 0.318$ ($\beta^* = 3.145$) with method III.

4.3.3. FCC crystal

The free energy of the fcc crystal structure was evaluated using the *Einstein molecule approach* described in section 3.2. We applied the method at two temperatures and at two different pressure values each, in order to be able to check thermodynamic consistency. We evaluated the free energy at the following state points (for the determination of the appropriate value for the coupling parameter Λ_E, see Appendix A.4):

- $T^* = 0.096$ with pressure values $p_1^* = 2.864$ and $p_2^* = 5.092$ ($\Lambda_E = 80000$)

- $T^* = 0.127$ with pressure values $p_1^* = 3.183$ and $p_2^* = 5.092$ ($\Lambda_E = 60000$)

As described in section 3.2, simulations performed with the Einstein molecule method are NVT simulations.

For the evaluation of both ΔA_1 (see equation (3.57)) and ΔA_2 (see equation (3.61)), the number of required Monte Carlo steps is in the order of 5×10^5. The result for the dependence of the chemical potential on the pressure for temperature $T^* = 0.127$ will be shown in figure 4.18 in section 4.4.

Consistency checks

Since we evaluated the free energy at two different pressure values, we could use the thermodynamic consistency check in order to verify our results and minimize the risk of unnoticed mistakes. The following table summarizes the results for each state point and shows the deviation in free energy:

p^*	T^*	ρ	A^*_{sol}	A^*_{sol} from TDI	$\Delta A^*/A^*$
3.183	0.127	1.3605	2.5111	2.4992	0.0048
5.092	0.127	1.3678	2.6253	2.6369	0.0044

4.3.4. Layered solid

Obtaining the free energy of the layered solid structure is very challenging. As already described in section 4.1, the solid is formed by layers that are separated by a relatively large distance. This large spatial separation leads to a very weak interaction between the layers. Consequently, free energy calculations for this structure are hard to tackle with thermodynamic integration schemes that rely on a reference structure. In particular, the *Einstein molecule approach* fails for the layered solid structure: due to the weak interaction between the layers, they can slide easily with respect to each other without significant change in potential energy. This issue causes a divergence of the integrand of ΔA_2 in equation (3.61) for low values of Λ_{E} (details on this correlation can be found in reference [4]), making it difficult to evaluate the integral numerically.

However, since we performed the direct coexistence method (see section 3.3) for obtaining the coexistence point between the layered solid and the fluid, we could use the coexistence point obtained from these calculations in order to evaluate the free energy of the layered solid at this point by taking advantage of the fact that at coexistence, both the fluid and the layered solid have the same chemical potential $\mu^*(p^*)$.

Since we had already calculated the chemical potential of the fcc lattice at temperature $T^* = 0.127$, we used the coexistence point $(T^* = 0.127, p^* = 0.487)$ (see results in section 4.4.3) for the evaluation of the chemical potential of the layered solid. In order to obtain the chemical potential of the fluid at temperature $T^* = 0.127$, we used the results from the simulations at $\beta^* p^* = 4$ (see subsection 4.3.1). Since the corresponding pressure in the respective simulation is $p^* = \frac{4}{\beta^*} = 0.508$, we had to perform thermodynamic integration along the isotherm at $T^* = 0.127$ to the density that corresponds to the desired pressure $p^* = 0.487$.

We obtained a value $\mu^* = 1.5614$ for the chemical potential of the fluid and the layered solid at their coexistence point. This value could then be used as a reference for thermodynamic integration along the isotherm $T^* = 0.127$ for the layered solid to obtain the dependence of the chemical potential on the pressure.
The result will shown in figure 4.18 of section 4.4 together with the chemical potential of the fcc structure.

4.4. Coexistence points

After evaluating the free energy for a certain state point with the methods specified in the above sections, we can use thermodynamic integration (see section 3.1) in order to integrate to any other state point. Linking the chemical potential curves $\mu^*(p^*)$ for two phases, we obtain the coexistence pressure p^*_{coex} at the desired temperature T^*_{coex}. Alternatively, when doing the direct coexistence method as described in 3.3, we directly obtain the coexistence pressure.

4.4.1. Fluid - fccp
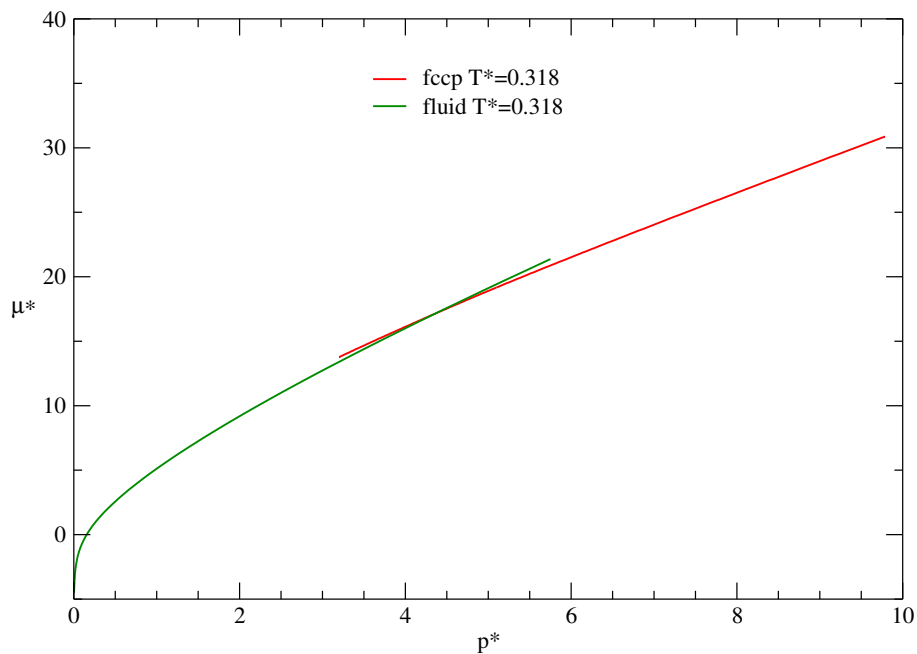
Figure 4.12.: Chemical potentials $\mu^*(p^*)$ for both the fccp and the fluid phase at $T^* = 0.318$ (as labeled); the coexistence is found to be $p^*_{\mathrm{coex}} = 4.352$.

Since we evaluated the free energy for both the fluid and the fccp structure at temperature $T^* = 0.318$, we could intersect the respective chemical potential curves $\mu^*(p^*)$ by integrating to the density range of interest and evaluating the pressure values from the respective equations of state. The intersection point of those two

curves is the coexistence point $(T^*_{\text{coex}}, p^*_{\text{coex}})$ for the two respective phases (see figure 4.12). At temperature $T^*_{\text{coex}} = 0.318$ the fluid and the fccp crystal coexist at pressure $p^*_{\text{coex}} = 4.352$. This point provided the initial value for the Gibbs Duhem integration, see section 3.4.

4.4.2. fcc - fccp

In general - due to hysteresis effects - it is not advisable to use NpT simulations at different temperatures in order to determine the location of a coexistence point. In cases where the two competing phases have a very similar structure, hysteresis effects are smaller than the error expected in free energy calculations.

This is the case for the transition between the ordered and the plastic fcc crystal. At the coexistence point, the transition from one structure to the other is realized without large hysteresis effects.
We performed simulations at pressure values $p^* = 5.092$ and $p^* = 6.365$. These isobars allowed us to localize the coexistence pressure by identifying discontinuities in the internal energy U^*. We performed two sets of simulations for each pressure - the first one serving as a rough estimate of the coexistence temperature (examining temperature increments in the order of $\Delta T^* = 10^{-3}$) and the second one - performed with smaller temperature increments (in the order of $\Delta T^* = 10^{-4}$) - in order to closely inspect the transition point and to examine possible hysteresis effects.

While at $p^* = 6.365$ the isobars exhibit some hysteresis (the coexistence temperature [4] lies between $0.173 < T^* < 0.176$), at $p^* = 5.092$, no hysteresis effects were visible and the coexistence temperature could be identified at $T^*_{\text{coex}} = 0.166$. This coexistence point was used as a basis for Gibbs Duhem integration (see section 3.4) in order to obtain the coexistence line between the fcc and the fccp structures.

Figures 4.13 and 4.14 show our results for the isobaric simulations at both pressures (each shown for the rough and the fine temperature grid). In these simulations, we used 3×10^5 Monte Carlo steps.

---

[4]The results from Gibbs Duhem integration suggest a coexistence temperature of $T^*_{\text{coex}} = 0.174$ at pressure $p^* = 6.365$, which lies well inside the hysteresis loop visible in figure 4.14.
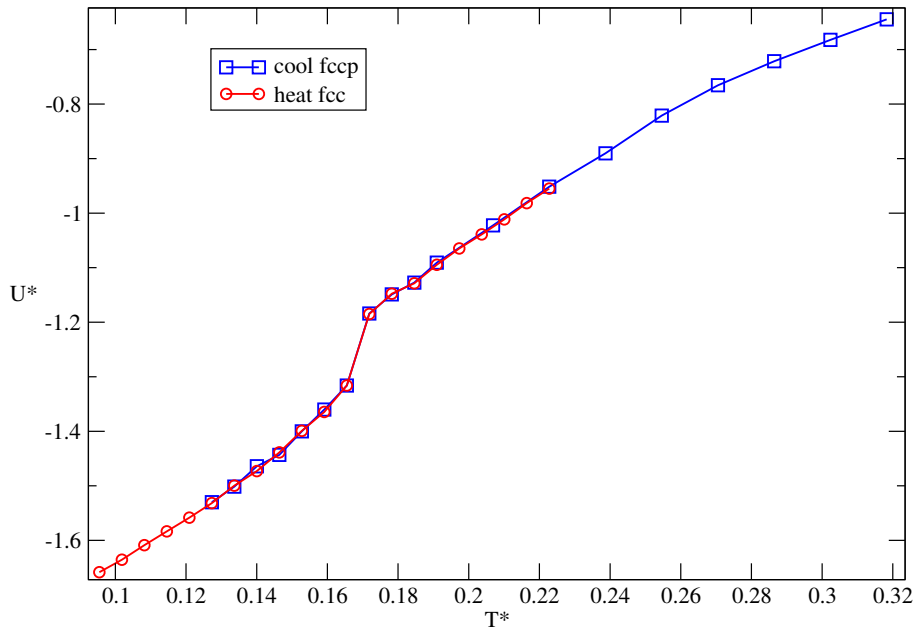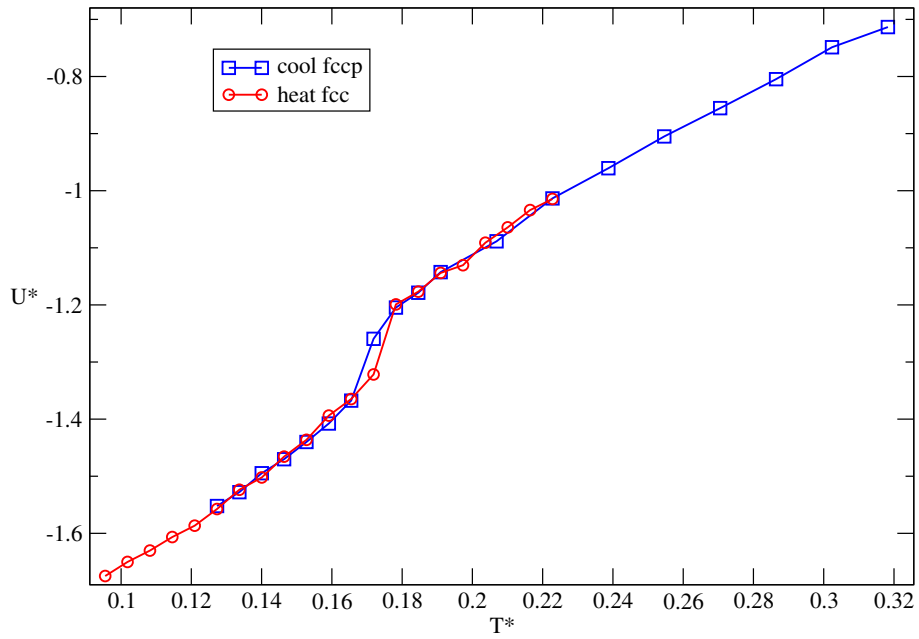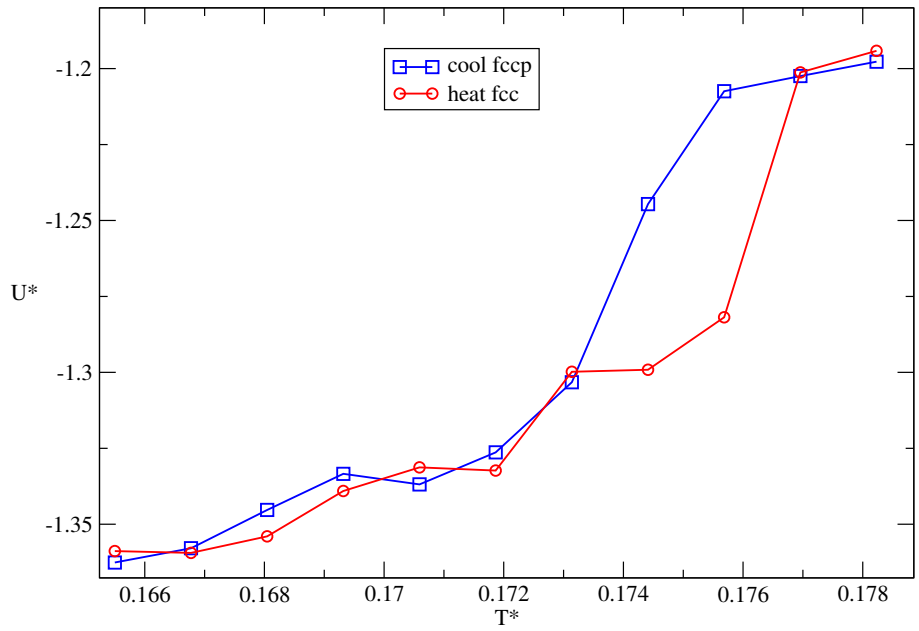
(a)
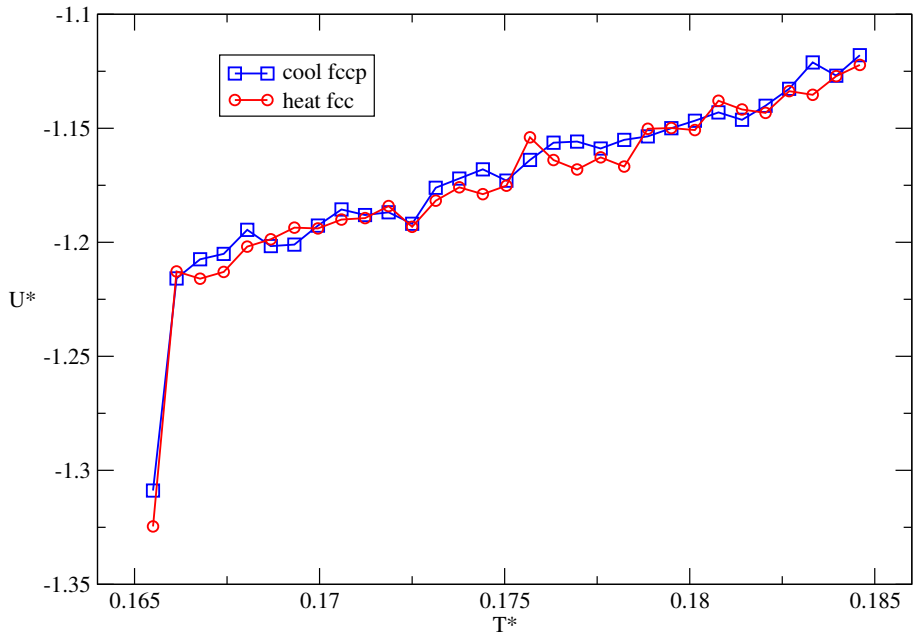
(b)

Figure 4.13.: Internal energy U^* of the fcc and the fccp at $p^* = 5.092$ and different temperatures T^*; plots show cooling of fccp structure (blue curves) and heating of the fcc structure (red curves) both for a rough (top panel) and a fine (bottom panel) temperature grid; no hysteresis effects are visible, the coexistence temperature was identified as $T^*_{\mathrm{coex}} = 0.166$

Figure 4.14.: Internal energy U^* of the fcc and the fccp at $p^* = 6.365$ and different temperatures T^*; plots show cooling of fccp structure (blue curves) and heating of the fcc structure (red curves) both for a rough (top panel) and a fine (bottom panel) temperature grid; isobars show significant hysteresis; transition occurs between $0.173 < T^* < 0.176$.

As already explained in subsection 4.2.2, a suitable way of defining the transition point between the ordered fcc and the fccp structures is to evaluate the angular distribution function $P(\theta)$, which is a measure of the orientational order of the particles. Figure 4.15 shows this angular distribution function for four temperatures evaluated at $p^* = 5.092$.
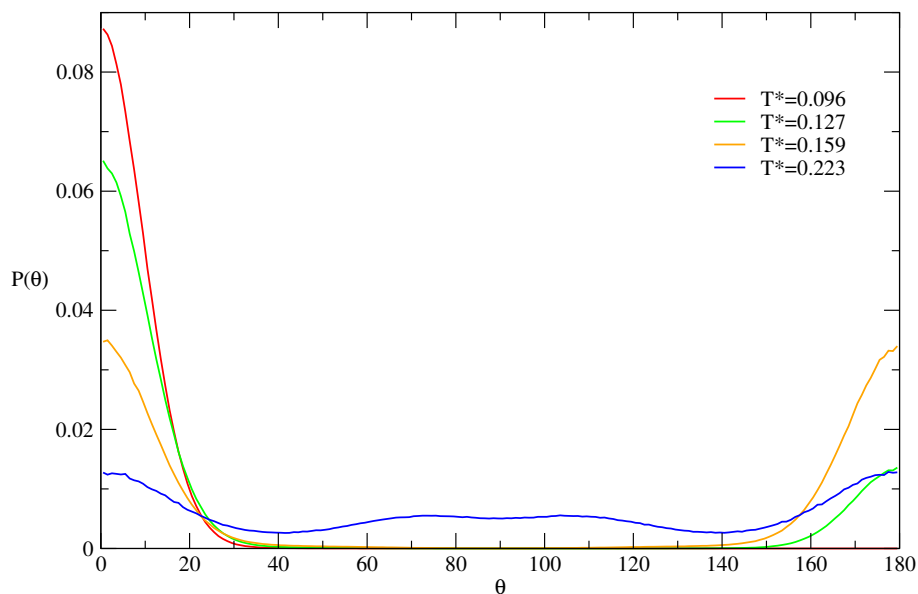
Figure 4.15.: Angular distribution function $P(\theta)$ for in the fcc - fccp transition at $p^* = 5.092$ and different temperatures (as labeled); depicted is the probability that the orientation of a particle encloses the angle θ with the orientation of its respective particle in the ordered fcc structure.

The red line, corresponding to the lowest temperature $T^* = 0.096$, exhibits the typical fcc peak at $\theta = 0\,^\circ$ already discussed in subsection 4.2.2 for figure 4.9. At $T^* = 0.127$ (green line), the particles become more detached from their original orientation, so some particles reverse their orientation, leading to the small peak at $\theta = 180\,^\circ$. At $T^* = 0.159$ (yellow line), the two peaks at $\theta = 0\,^\circ$ and $\theta = 180\,^\circ$ have approximately attained the same height. At even higher temperatures ($T^* = 0.223$, blue line), the fcc lattice has fully transformed into the fccp structure, where the particles have a relatively uniform orientational distribution, still with a slight preference for the direction of the particles in the ordered fcc crystal.

A comparison of figure 4.15 with figure 4.9 in subsection 4.2.2 points out the

difference between the angular distribution function of the fccp crystal and the fully uniform angular distribution function of the particles in the fluid phase.

4.4.3. Fluid - Layered solid

Due to the particular structure of the layered solid (see subsection 4.3.4), of the methods introduced in chapter 3, the direct coexistence method was initially the only method that could be applied.

The special technique described in section 3.3 for structures prone to premelting [13] proved to be a suitable tool to evaluate an initial coexistence point between the layered solid and the fluid.

Because of the unique visual nature of the layered solid, the configurations resulting from the direct coexistence simulations can be adequately analyzed by visual inspection.

Simulations were performed at temperatures $T^* = 0.127$ and $T^* = 0.159$, over a pressure range of $0.064 \leq p^* \leq 1.591$. Figures 4.17 and 4.16 show snapshots of the configurations after roughly 6×10^6 Monte Carlo steps for temperatures $T^* = 0.127$ and $T^* = 0.159$ and for pressure values above, below and very close to the coexistence pressure. It is evident that at higher temperatures, the dynamics of the simulations are faster. At $T^* = 0.159$, all shown configurations except the one close to the coexistence pressure ($p^* = 1.591$) had completely transformed into either a fluid or a solid. In contrast, at $T^* = 0.127$, after the same amount of Monte Carlo steps, the configurations were clearly transforming into one phase or the other, but had not fully transformed yet.

While figures 4.17 and 4.16 show snapshots of the first simulations serving as rough estimates for the coexistence pressure p^*_{coex}, we have also performed similar simulations using a much finder grid in pressure (about $\Delta p^* \approx 0.1 - 0.2$) in order to bracket the coexistence pressure.
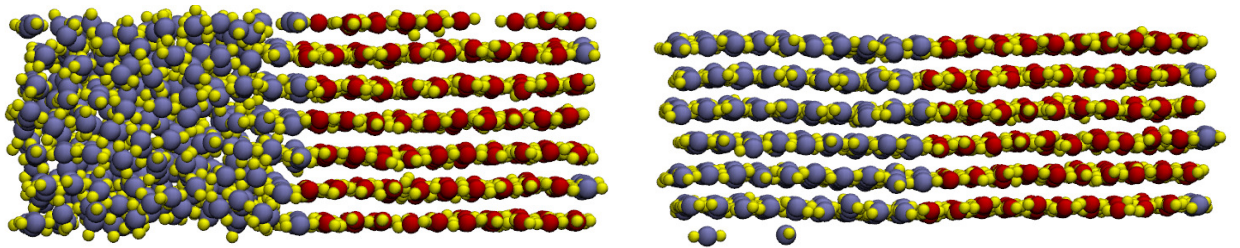
For $T^* = 0.159$, we have found the coexistence pressure to be located in the interval $1.591 < p^*_{\text{coex}} < 1.600$ and have used the value $p^*_{\text{coex}} = 1.595$ for subsequent Gibbs-Duhem integration.
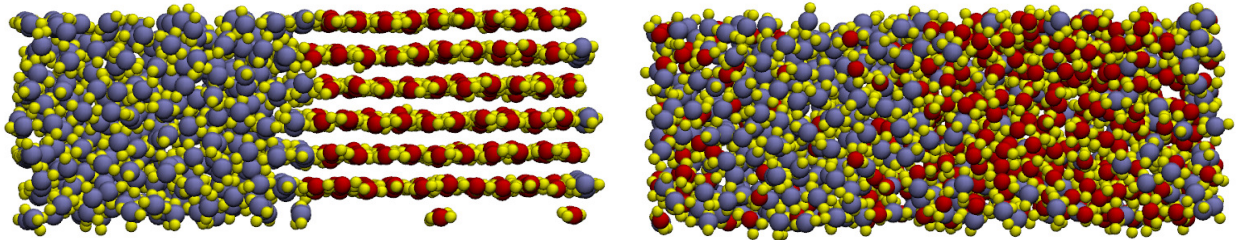
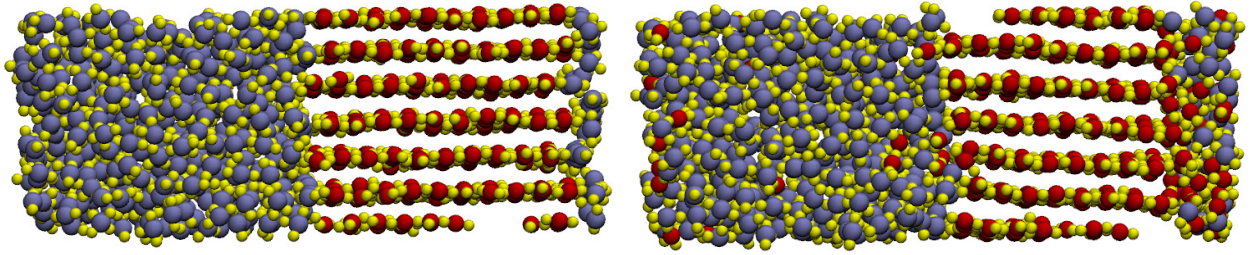(a) $T^* = 0.159$, $p^* = 1.400$
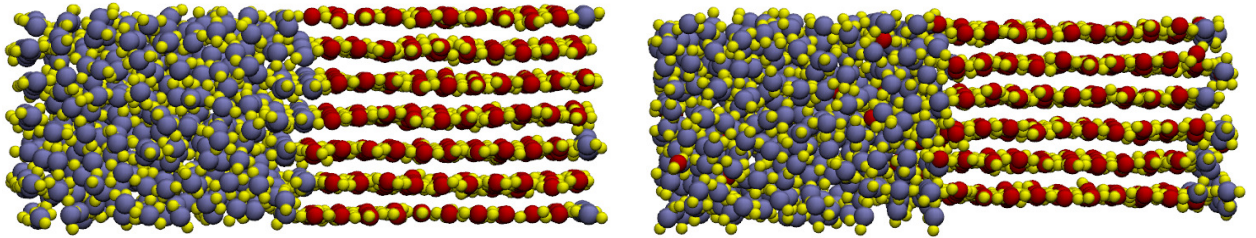
(b) $T^* = 0.159$, $p^* = 1.591$

(c) $T^* = 0.159$, $p^* = 1.719$
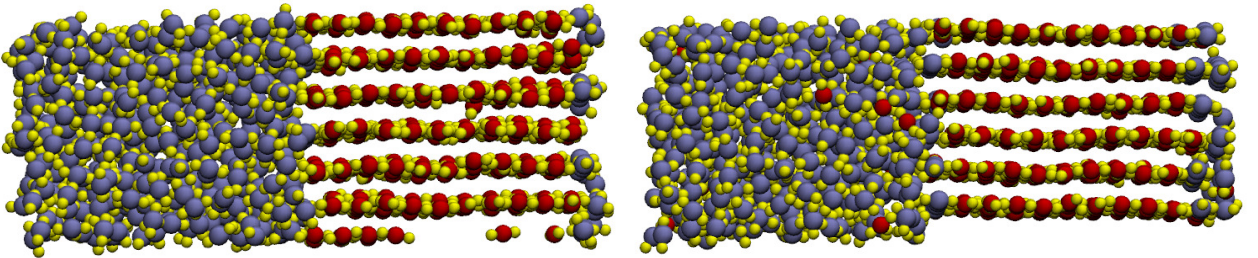
Figure 4.16.: Snapshots of direct coexistence simulations of the layered structure and the fluid phase at coexistence at $T^* = 0.159$ and different pressure values (as specified); left panels: initial configurations; right panels: configurations after roughly 6×10^6 Monte Carlo steps.

For $T^* = 0.127$, we could only locate the transition pressure in the interval $0.464 < p^*_{\text{coex}} < 0.500$ from the direct coexistence simulations on the finer pressure grid. This is due to the fact that these simulations need a very large amount of steps in order to clearly evolve into one phase or the other. However, the coexistence line resulting from Gibbs-Duhem integration suggests a coexistence pressure of $p^*_{\text{coex}} = 0.487$.

(a) $T^* = 0.127$, $p^* = 0.446$

(b) $T^* = 0.127$, $p^* = 0.509$
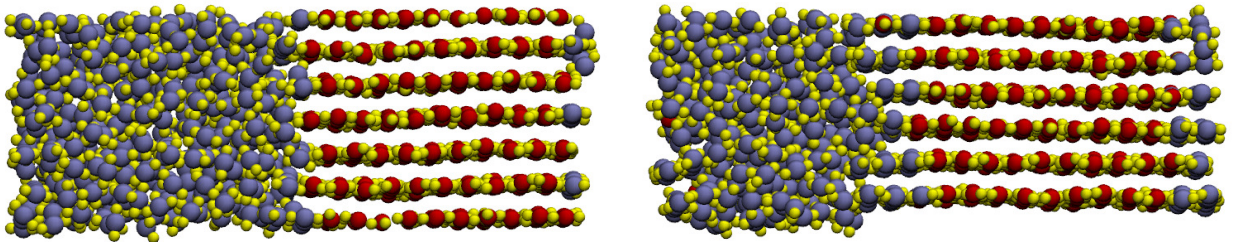
(c) $T^* = 0.127$, $p^* = 0.637$

Figure 4.17.: Snapshots of direct coexistence simulations of the layered structure and the fluid phase at coexistence at $T^* = 0.127$ and different pressure values (as specified); left panels: initial configurations; right panels: configurations after roughly 6×10^6 Monte Carlo steps.

4.4.4. Layered solid - fcc

It was not possible to calculate the free energy of the layered solid via direct cal-
culation methods (as explained in subsection 4.3.4). However, as soon as we had
obtained an initial coexistence point between the layered solid and the fluid with
the direct coexistence method, we could calculate the dependence of the chemical
potential of the layered solid on the pressure (the details of this calculations are
explained in subsection 4.3.4).

Consequently, we obtained the coexistence point at temperature $T^* = 0.127$ be-
tween the layered solid and the fcc structure (the latter via the *Einstein molecule
approach*, see 4.3.3), by intersecting their chemical potential curves $\mu^*(p^*)$.

Figure 4.18 shows the chemical potentials $\mu^*(p^*)$ for both the layered solid and the
fcc. Their intersection point yields the coexistence pressure $p^*_{\text{coex}} = 2.746$.
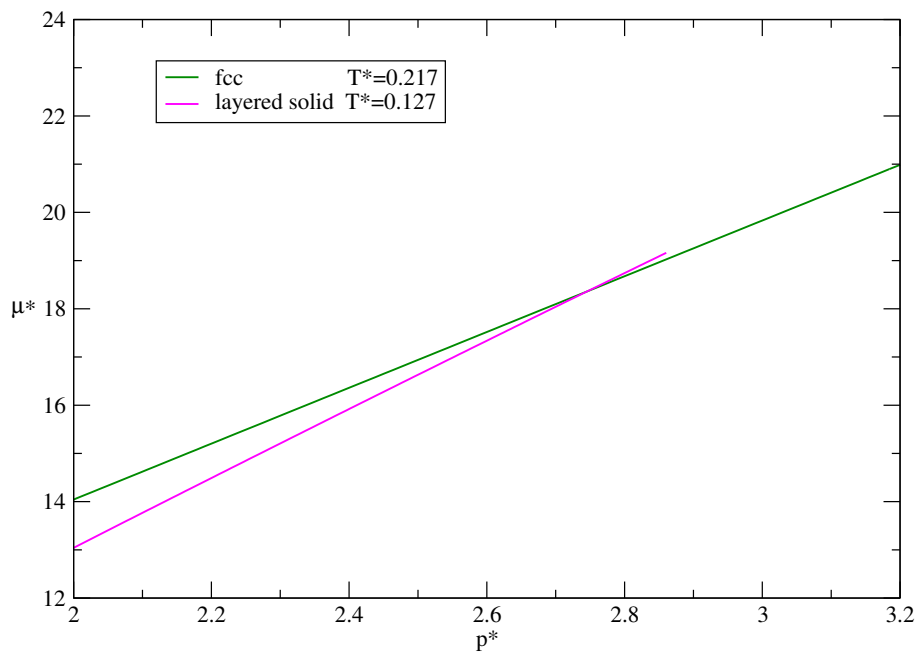
Figure 4.18.: Chemical potentials $\mu^*(p^*)$ for both the layered solid and the fcc
structure at $T^* = 0.127$; the coexistence point is located at $p^* =
2.746$.

4.5. Phase diagram

From the simulations described throughout section 4.4, we obtained five coexistence lines using Gibbs-Duhem integration (see section 3.4). Combining these curves yields the **phase diagram** of the specific system of IPCs that we studied in this thesis. Figure 4.19 depicts this phase diagram in the (p^*, T^*) plane.

It exhibits two triple points:

A layered solid - fcc - fccp ($p^* = 2.991, T^* = 0.152$)

B fluid - layered solid - fccp ($p^* = 2.860, T^* = 0.189$)
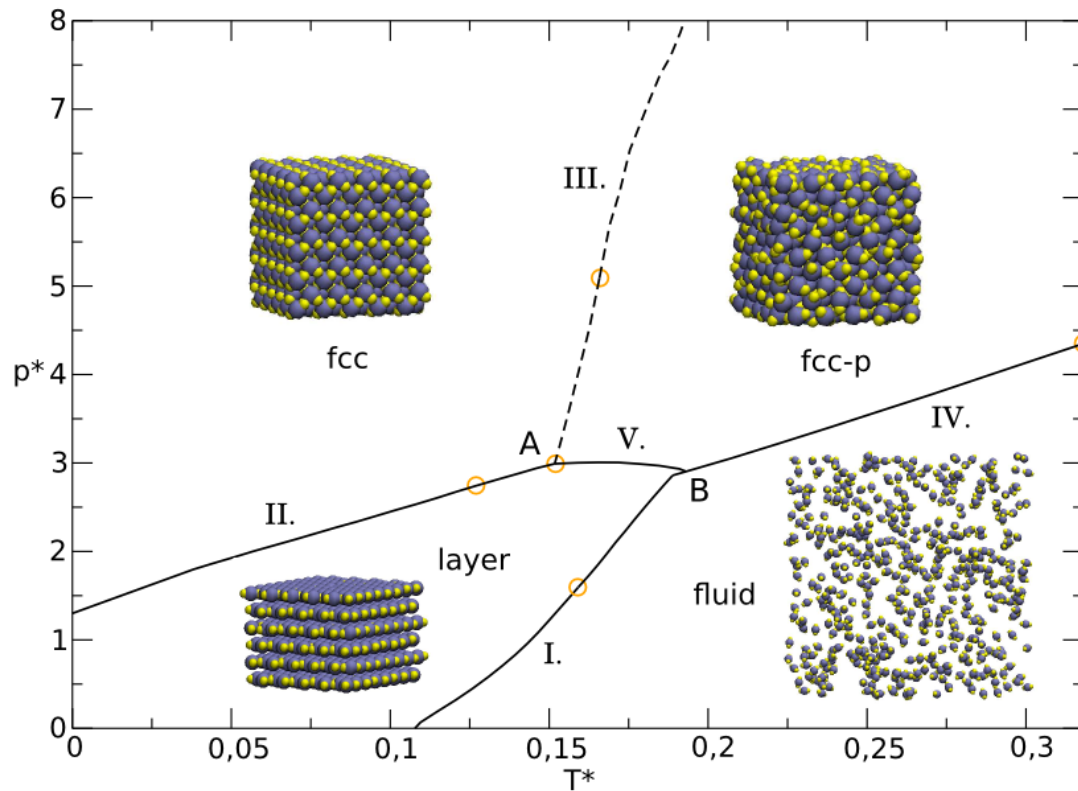
Figure 4.19.: Equilibrium phase diagram of the IPC system with the parameters defined in table 2.1, depicted in the (p^*, T^*) plane; initial coexistence points are marked with orange circles; the two triple points are marked with "A" and "B" (as defined above).

In the following, we summarize the process of calculating the coexistence lines labeled I.-V. in figure 4.19. Some simple consistency tests were applied in order to confirm our results.

I. fluid - layered solid:

We obtained the initial coexistence point ($T^* = 0.159$, $p^* = 1.595$) from direct coexistence simulations (see sections 3.3 and 4.4.3). The coexistence line resulting from Gibbs-Duhem integration (depicted in figure 4.19) confirms the other coexistence point localized in the interval $0.464 < p^* < 0.500$ during the simulations at $T^* = 0.127$.

II. layered solid - fcc:

For the layered solid and the fcc lattice, we used the condition of equal chemical potential at coexistence in order to evaluate their coexistence point (see section 4.4.4). The chemical potential of the layered solid was obtained by thermodynamic integration from the coexistence point of this structure with the fluid. There, the chemical potential of the layered solid is known, since - because of the condition of equal chemical potentials at coexistence - it is the same as that of the fluid (see section 4.3.4). The chemical potential of the fcc structure was evaluated using the *Einstein molecule approach* (see sections 3.2 and 4.3.3). The initial coexistence point was located at ($T^* = 0.127$, $p^* = 2.746$). At low temperatures, the coexistence line shown in figure 4.19 approaches the coexistence pressure value obtained at $T \to 0$ with the evolutionary algorithm [11] that was employed to predict candidate structures (see section 4.1). This pressure value is $p^* = 1.2998$.

III. fcc - fccp:

The initial coexistence point between the fcc and the fccp structures was obtained by heating the fcc lattice and cooling the fccp lattice (see section 4.4.2). Those simulations only exhibited small hysteresis loops, so the coexistence point could be obtained with good accuracy to ($T^* = 0.166$, $p^* = 5.092$). For the other pressure value imposed in those simulations ($p^* = 6.365$) the coexistence line shown in figure 4.19 suggests a coexistence temperature of $T^* = 0.174$; although this temperature lies in the interval predicted by our simulations described in section 4.4.2, the coexistence has to be recalculated, since it exhibits some significant inaccuracies:

During Gibbs-Duhem simulations, two independent NpT simulations of both competing phases were performed (see section 3.4). In the case of the fcc - fccp coexistence line, for a significant number of points along the coexistence line, the resulting configurations are not distinguishable. This means that the resulting line deviates from the actual phase boundary (presumably entering the region of thermodynamic stability of the fccp lattice).

IV. fccp - liquid:

The initial coexistence point ($T^* = 0.318$, $p^* = 4.352$) of the fccp structure and the fluid was obtained via the condition of equal chemical potential at the coexistence point (see section 4.4.1). The chemical potential of the fccp plastic crystal was evaluated using thermodynamic integration along a path of $\beta^* p^* = const.$ (see section 4.3.2), while in the case of the fluid phase, the chemical potential was obtained by thermodynamic integration from the ideal gas (see section 4.3.1).

V. fccp - layered solid:

For the evaluation of the coexistence line between the fccp structure and the layered solid, we used triple point **A** as the initial coexistence point. However, the error in coexistence line III. transfers to the calculation of this coexistence line. This is obvious in the visualisation of the phase diagram, since the triple point **B** does not lie exactly on coexistence line V., see figure 4.19.

5. Conclusion and Outlook

In this thesis, we evaluated the regions of stability for four phases exhibited by a specific system of inverse patchy colloids (IPCs) and the respective coexistence lines. IPCs are mutually repulsive colloidal particles carrying two patches on their poles, which repel each other and attract the "naked" parts of the colloid. These features result in a highly anisotropic and selective interaction between two IPCs that - depending on their relative orientation - can either be attractive or repulsive.

We started our calculations of the equilibrium phase diagram with two ordered candidate structures that had been predicted for vanishing temperatures with an optimisation technique based on evolutionary algorithms [11]: one of those solids is a fcc structure, while the other is composed of two-dimensional layers separated by a relatively large spacing. From those structures, we started simple Monte Carlo simulations, exploring their melting and freezing behaviour as well as their behaviour under increasing and decreasing pressure. Those simulations gave us a first idea of the stability regions of the respective phases. Furthermore, we discovered that the fcc structure is also stable as a plastic crystal in certain temperature and pressure ranges.

We then performed free energy calculations, employing a different calculation technique for each phase, since they differ significantly in their properties:

(i) For the fluid phase and the plastic fcc crystal, we used thermodynamic integration schemes that rely on reference structures of known free energy, such as the hard sphere system or the ideal gas.

(ii) For the ordered fcc crystal, we computed the free energy via the *Einstein molecule approach* [4].

(iii) Due to the particular structure of the layered solid, both direct thermody-

namic integration from a reference state and the *Einstein molecule approach* failed due to the large spacing between the layers and the ensuing weak interaction between the layers. Layers can easily slide with respect to each other without significant change in potential energy, which is incompatible with the basic ideas of the Einstein molecule approach, in which the potential energy is determined by the translation of a particle with respect to its equilibrium position. Consequently, we focused on an accurate evaluation of the melting point of the layered solid by direct coexistence simulations, which, via the condition of equal chemical potentials at coexistence, provided a reference value for the free energy of the layered solid that could be used for thermodynamic integration to other state points.

Our free energy calculations allowed us to calculate coexistence points between the respective phases. Starting from these results, we could evaluate the full coexistence lines employing the Gibbs-Duhem thermodynamic integration method. Those results were found to be consistent with the predictions from our exploratory simulations. The coexistence lines between the phases allowed a general understanding of large parts of the equilibrium phase diagram. This phase diagram exhibits two triple points, one between the layered solid, the fcc and the fccp structure, the other one between the fccp structure, the fluid and the layered solid.

With this work, we have contributed to a deeper understanding of the IPC system we studied and provided thorough insight in the behaviour of its phases.

There are a number of issues that have to be addressed within future research efforts in order to confirm and even improve the results obtained in this thesis. First of all, it will be important to quantify errors and properly calculate their propagation in the results presented in this thesis. Error calculations are quite cumbersome in the context of free energy calculations, but should be performed in order to estimate the accuracy of the results obtained in this work.

Furthermore, a recalculation of the coexistence line between the plastic fccp crystal and the fcc crystal, which could not be computed to a desirable accuracy, will represent an important continuation of this work. To this end, the initial coexistence point has to be recalculated. In this thesis, we obtained an initial coexistence

point between these two structures by heating the fcc structure and cooling the fccp structure. The next logical step will be to compute the free energies of those two phases and evaluate their coexistence point via the condition of equal chemical potential at coexistence. In this context, proper error calculation will be very useful. In addition, due to the easy interconversion between the two phases, the possibility that Gibbs-Duhem integration might not work at all for this coexistence line has to be considered. In that case, the coexistence line will have to be traced using other methods, for example evaluation of several distinct coexistence points and interpolation between them.

Another interesting issue for further research efforts involving the system of IPCs will be to accurately locate the vapour-liquid transition that we encountered in this system, in order to get a more comprehensive picture of the phase diagram.

Since we studied the phase diagram for a certain set of parameters (see 2.1), it would be interesting to study the influence of a change in those parameters on the phase diagram, such as increasing or decreasing the size of the patches, or experimenting with the number of patches on a particle.

Considering the results obtained in this work and the possible features of IPC systems that are yet to be explored, it can be stated that IPCs form highly intriguing systems governed by their uniquely tunable, anisotropic interactions.

A. Appendix

A.1. Reduced Units

In this work, we express the internal energy U, the pressure p and the temperature T via reduced units. Those units are defined as follows:

$$U^* = \frac{U}{\varepsilon_{\min}}$$

$$p^* = \frac{p(2\sigma)^3}{\varepsilon_{\min}}$$

$$T^* = \frac{k_{\mathrm{B}}T}{\varepsilon_{\min}}$$

$$\beta^* p^* = \beta p \ (2\sigma)^3$$

where 2σ is the particles' diameter. As the unit of energy $\varepsilon_{\min}$ we use the energy of the EP configuration (see subsection 2.2), which also serves as a normalisation factor for the potential shown in figure 2.3 of section 2.3. Its value is

$$\varepsilon_{\min} = -15.71 \ k_{\mathrm{B}}T \quad .$$

A.2. Relation between ψ and the Euler angles

The dependence of the angle ψ, which is the angle the particle encloses with the orientation of its respective particle in the reference Einstein crystal, on the Euler angles θ, ϕ and γ can be understood in the following way:
The orientations of the IPCs are described via the vector $\hat{\boldsymbol{n}}$ (see section 2.2). For a given set of Euler angles $\{\theta, \phi, \gamma\}$ (i.e. a given orientation in space), we obtain

$\hat{\boldsymbol{n}}$ by applying the rotation matrix, which is given by

$$R = \begin{pmatrix} \cos\phi\cos\gamma - \sin\phi\cos\theta\sin\gamma & \sin\phi\cos\gamma + \cos\phi\cos\theta\sin\gamma & \sin\theta\sin\gamma \\ -\cos\phi\sin\gamma - \sin\phi\cos\theta\cos\gamma & -\sin\phi\sin\gamma + \cos\phi\cos\theta\cos\gamma & \sin\theta\cos\gamma \\ \sin\phi\sin\theta & -\cos\phi\sin\theta & \cos\theta \end{pmatrix}$$

to the orientational vector of the respective particle in the reference Einstein crystal, say $\hat{\boldsymbol{n}}_{\text{ref}}$, in the following way:

$$\hat{\boldsymbol{n}} = R(\theta, \phi, \gamma)\ \hat{\boldsymbol{n}}_{\text{ref}} \quad . \tag{A.1}$$

The angle determining the orientation of the particle, ψ, can then be obtained by evaluating the scalar product of the particle's orientational vector $\hat{\boldsymbol{n}}$ and its counterpart in the reference Einstein crystal, $\hat{\boldsymbol{n}}_{\text{ref}}$:

$$\cos\psi = \frac{\hat{\boldsymbol{n}} \cdot \hat{\boldsymbol{n}}_{\text{ref}}}{|\hat{\boldsymbol{n}}||\hat{\boldsymbol{n}}_{\text{ref}}|} \quad . \tag{A.2}$$

Thus, $\psi = \psi(\theta, \phi, \gamma)$ and $v_{\text{E,or}}(\psi) = v_{\text{E,or}}(\psi(\theta, \phi, \gamma)) = \Lambda_{\text{E}}\sin^2\psi(\theta, \phi, \gamma)$.

A.3. Derivation of the Gibbs-Duhem relation

The following derivation of the Gibbs-Duhem relation retraces the one given in reference [?].

We start from the fundamental thermodynamic relation

$$dU = TdS - pdV + \mu dN \quad . \tag{A.3}$$

The internal energy $U(S, V, N)$ is an extensive property, so

$$U(\alpha S, \alpha V, \alpha N) = \alpha\ U(S, V, N) \quad , \tag{A.4}$$

with α being a multiplicative factor by which the system is increased in size. Let us now consider an infinitesimal increase in system size ($\alpha = 1 + \varepsilon$, $\varepsilon \ll 1$):

$$U((1 + \varepsilon)S, (1 + \varepsilon)V, (1 + \varepsilon)N) = (1 + \varepsilon)\ U \quad . \tag{A.5}$$

Taylor expansion of the left side of the above expression yields:

$$U((1+\varepsilon)S, (1+\varepsilon)V, (1+\varepsilon)N) = U + \frac{\partial U}{\partial S}S\varepsilon + \frac{\partial U}{\partial V}V\varepsilon + \frac{\partial U}{\partial N}N\varepsilon + O(\varepsilon^2) \quad . \text{ (A.6)}$$

With the Maxwell relations

$$T = \frac{\partial U}{\partial S} \ , \qquad -p = \frac{\partial U}{\partial V} \ , \qquad \mu = \frac{\partial U}{\partial N} \tag{A.7}$$

and relation (A.5) we obtain

$$(\varepsilon + 1) \ U = U + \varepsilon(TS + pV + \mu N) + O(\varepsilon^2) \tag{A.8}$$

Subtracting U and dividing by ε yields:

$$U = TS + pV + \mu N + O(\varepsilon) \quad . \tag{A.9}$$

Finally, passing the limit $\varepsilon \to 0$, gives the *Euler equation*:

$$U = TS - pV + \mu N \quad . \tag{A.10}$$

We now take the total derivative of equation (A.10):

$$dU = TdS - pdV + \mu dN + SdT - Vdp + Nd\mu \quad . \tag{A.11}$$

Comparing this with the fundamental thermodynamic relation in equation (A.3), we find that:

$$SdT - Vdp + Nd\mu = 0 \quad , \tag{A.12}$$

which is the *Gibbs-Duhem relation*.

A.4. Choosing Λ_E for Einstein molecule simulations

When choosing the coupling parameter Λ_E for simulations within the *Einstein molecule approach* (see section 3.2), one has to find a compromise between two issues:

The procedure for calculating ΔA_1 (see subsection 3.2.2), which is the difference in free energy between the ideal Einstein crystal and the interacting Einstein crystal, relies on the fact that the two systems only differ slightly in their properties

(for details on this, see reference [4]). Thus, the coupling parameter Λ_{E}, which determines the strength of the coupling to the particles' equilibrium positions and orientations, should be as large as possible.

On the other hand, we are interested in keeping the domain of integration when evaluating ΔA_2 (equation 3.57) as small as possible, thus reducing the error in our calculation.

A way of determining a suitable value for the coupling parameter is to perform several calculations of A_{sol} (see section 3.2) with increasing values of coupling parameter. For Λ_{E}-values that are too small, the free energy will change considerably upon further increasing the coupling parameter. However, in a certain range, the free energy A_{sol} converges to a constant value, *i.e.* does not change anymore upon further increasing the coupling parameter.

The best choice for Λ_{E} is the lowest value for which the free energy has converged to the constant number found in the exploratory runs described above.

Bibliography

[1] R. Blaak E. Bianchi and C. N. Likos. Patchy colloids: state of the art and perspectives. *Phys. Chem. Chem. Phys.*, 13:6397, 2011.

[2] A. B. Pawar and I. Kretzschmar. Fabrication, assembly, and application of patchy particles. *Macromol. Rapid. Commun.*, 31:150, 2010.

[3] G. Kahl E. Bianchi and C. N. Likos. Inverse patchy colloids: from microscopic description to mesoscopic coarse-graining. *Soft Matter*, 7:8313, 2011.

[4] J. L. F. Abascal C. Vega, E. Sanz and E. G. Noya. Determination of phase diagrams via computer simulation: methodology and applications to water, electrolytes and proteins. *Condens. Matter*, 20:153101 (38pp), 2008.

[5] C. Vega E. G. Noya and E. de Miguel. Determination of the melting point of hard spheres from direct coexistence simulation methods. *J. Chem. Phys.*, 128:154507, 2008.

[6] R. Blaak C. N. Likos and A. Wynveen. Computer simulations of charged star polymers and brushes. *J. Phys.: Condens. Matter*, 20:494221, 2008.

[7] P. Debye and E. Hueckel. Zur Theorie der Elektrolyte. *Physikalische Zeitschrift*, 24:185–206, 1923.

[8] B. van Oorschot D. Pelt F. Smallenburg L. Filion, M. Marechal and M. Dijkstra. Efficient method for predicting crystal structures at finite temperature: Variable box shape simulations. *Phys. Rev. Lett.*, 103:188302, 2009.

[9] G. Kahl D. Gottwald, C. N. Likos and H. Lwen. Phase behavior of ionic microgels. *Phys. Rev. Lett.*, 92:68301, 2004.

[10] G. J. Pauschenwein and G. Kahl. Clusters, columns, and lamellae - minimum energy configurations in core softened potentials. *Soft Matter*, 4:1396, 2008.

[11] E. Bianchi G. Doppelbauer, E.G. Noya and G. Kahl. Self-assembly scenarios of patchy colloidal particles. *Soft Matter*, 8:7768, 2012.

[12] D. Frenkel and A. J. C. Ladd. *J. Chem. Phys.*, 81:3188, 1984.

[13] J. W. M. Frenken B. Pluis, A. W. Denier van der Gon and J. F. van der Veen. Crystal-face dependence of surface melting. *Phys. Rev. Lett.*, 59:2678–2681, 1987.

[14] D. A. Kofke. Direct evaluation of phase coexistence by molecular simulation via integration along the saturation line. *J. Chem. Phys.*, 98:4149, 1993.

[15] D. Frenkel and B. Smit. *Understanding Molecular Simulation*. Academic Press, 2002.

[16] J. Kolafa. Nonanalytical equation of state of the hard sphere fluid. *Phys. Chem. Chem. Phys.*, 8:464–468, 2006.

[17] K. R. Hall. Another hard-sphere equation of state. *J. Chem. Phys.*, 57:2252, 1972.

Acknowledgements